Journal of Applied Physics

Pyroelectric infrared detectors and materials—A critical perspective

Cite as: J. Appl. Phys. **133**, 080902 (2023); https://doi.org/10.1063/5.0141044
Submitted: 02 January 2023 • Accepted: 05 February 2023 • Published Online: 24 February 2023
Published open access through an agreement with JISC Collections

Roger W. Whatmore and Samuel J. Ward

COLLECTIONS

This paper was selected as an Editor's Pick

View Online Export Citation CrossMark

ARTICLES YOU MAY BE INTERESTED IN

Controlling quantum phases of electrons and excitons in moiré superlattices
Journal of Applied Physics **133**, 080901 (2023); https://doi.org/10.1063/5.0139179

Tunable Fano resonance in coupled topological one-dimensional photonic crystal heterostructure and defective photonic crystal
Journal of Applied Physics **133**, 083102 (2023); https://doi.org/10.1063/5.0135235

A reconfigurable asymmetric-transmission metasurface for dynamic manipulation of transmission, reflection, and polarization
Journal of Applied Physics **133**, 083101 (2023); https://doi.org/10.1063/5.0134540

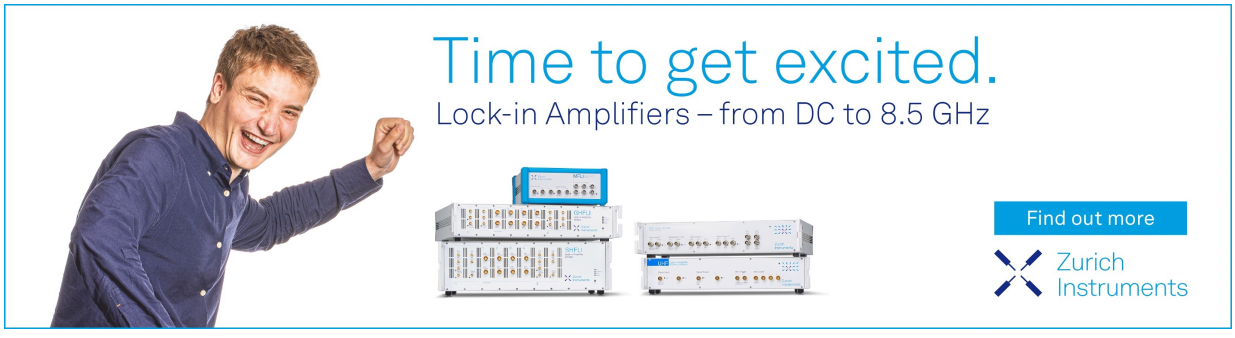

© 2023 Author(s).

AIP Publishing

Journal of Applied Physics PERSPECTIVE scitation.org/journal/jap

Pyroelectric infrared detectors and materials—A critical perspective

Cite as: J. Appl. Phys. 133, 080902 (2023); doi: 10.1063/5.0141044
Submitted: 2 January 2023 · Accepted: 5 February 2023 ·
Published Online: 24 February 2023

View Online Export Citation CrossMark

Roger W. Whatmore[a] and Samuel J. Ward

AFFILIATIONS

Department of Materials, Faculty of Engineering, Imperial College London, London SW7 2AZ, United Kingdom

[a]Author to whom correspondence should be addressed: r.whatmore@imperial.ac.uk

ABSTRACT

Pyroelectric infrared detectors (PIRDs) have a number of advantages over other IR sensors, including room-temperature operation, wide wavelength sensitivity, and low cost, leading to their use in many applications and a market expected to reach U.S.$68 million by 2025. Physical models that can be used to accurately predict the performances of PIRDs of different types are reviewed in detail. All polar dielectrics exhibit the pyroelectric effect, so there are many materials potentially available for use in PIRDs. Traditionally, a range of "figures-of-merit" (FoMs) are employed to aid the selection of the best material to use in a given application. These FoMs, and their utility in determining how a given pyroelectric material will behave in a PIRD, are reviewed in the light of the physical models and the availability of dielectric data, which cover the frequency ranges of greatest interest for PIRDs (0.1–100 Hz). The properties of several pyroelectric materials are reviewed, and models are derived for their dielectric properties as functions of frequency. It is concluded, first, that the availability of full-frequency dielectric data is highly desirable if accurate predictions of device performance are to be obtained from the models and that second, the FoMs have practical utility in only very limited circumstances. Thus, they must be used with considerable care and circumspection. The circumstances under which each FoM is likely to give a good prediction for utility are discussed. The properties of some recently researched pyroelectric materials, including lead-containing single crystals in the $Pb[(Mg_{1/3}Nb_{2/3})_xTi_{1-x}]O_3$ system and $Na_{1/2}Bi_{1/2}TiO_3$–$K_{1/2}Bi_{1/2}TiO_3$ based lead-free crystals and ceramics, are reviewed in the light of this, and their properties and potential for device applications compared with the industry-standard material, $LiTaO_3$. It is concluded that while there is potential for significant device performance improvements by using improved materials, especially with the PMN-PT-based materials, factors such as temperature stability, uniformity, and ease-of-processing are at least as important as device performance in determining material utility. The properties reported for the new lead-free materials do not, as yet, promise a performance likely to compete with $LiTaO_3$ for mm-scale detectors, a material that is both readily available and lead-free.

© 2023 Author(s). All article content, except where otherwise noted, is licensed under a Creative Commons Attribution (CC BY) license (http://creativecommons.org/licenses/by/4.0/). https://doi.org/10.1063/5.0141044

I. INTRODUCTION

Polar dielectrics are insulating materials whose crystal structures both lack a center-of-symmetry (are "acentric") and possess a unique symmetry axis. All polar dielectrics will exhibit the pyroelectric effect when the temperature is changed, which is the appearance of electrostatic charge on a surface for which the plane normal has a non-zero component parallel to the polar axis.

The effect is illustrated in Fig. 1(a). In this schematic structure, there are parallel layers of cations and anions, with the cations displaced along the polar z axis by an amount δ relative to the charge-neutral positions (designated by the lines O–O) between the layers of anions. This creates an electric dipole moment which we define as spontaneous polarization P_S. The displaced position of the cation layers means that they sit within an asymmetric potential well [see Fig. 1(b)]. As the temperature increases, the vibrational amplitudes of the cations within this well will increase, and their mean positions will tend to move back toward the charge-neutral plane O–O. This changes the value of P_S and gives rise to the pyroelectric effect. We define the pyroelectric coefficient $p(\Theta)$ as [see Fig. 1(c)]

$$p(\Theta) = \frac{dP_S}{d\Theta}, \tag{1}$$

where Θ is the absolute temperature. If a slab of a pyroelectric material with electroded major faces (area A) and short-circuited

© Author(s) 2023

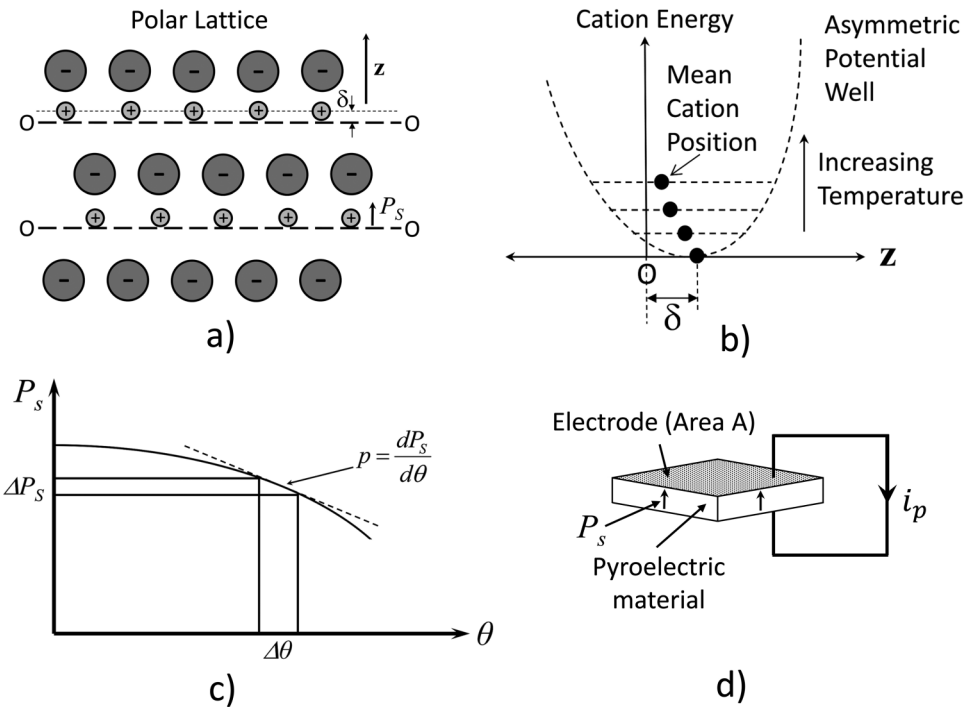

FIG. 1. Polar crystal structures and pyroelectricity: (a) a structure in which layers of cations are displaced along the z axis by an amount δ relative to the charge-neutral position O–O; (b) how the mean cation position (δ) changes with temperature, which gives rise to the pyroelectric effect; (c) the definition of the pyroelectric coefficient as a change in spontaneous polarization (P_S) as a function of temperature (θ); (d) a slab of pyroelectric materials with electroded major faces with area A, the electrodes are short-circuited and a pyroelectric current i_p generated by a rate of change of temperature $\frac{d\theta}{dt}$.

electrodes [Fig. 1(d)] is subjected to a change in temperature, then a pyroelectric current i_p will flow in the external circuit. i_p is given by

$$i_p = Ap\left(\frac{d\theta}{dt}\right), \tag{2}$$

where θ is the temperature difference between the element and its surroundings and $\frac{d\theta}{dt}$ is the rate of change of θ with time t. p represents the component of $p(\Theta)$ along the electrode plane normal, acknowledging that it is dependent on Θ. In most pyroelectric devices, the electrode surface plane normal is arranged to be parallel to the polar axis, but in certain circumstances, there may be some advantages to making these two vectors non-parallel.[1,2] This possibility will not be discussed further in this paper.

Lang[3] has pointed out that the first description of observable phenomena that can be ascribed to pyroelectricity can be traced back as far as the Greek philosopher Theophrastus (c371–c287 BCE). The electrostatic effects of pyroelectricity were studied by such historically famous scientists as Linneus, Brewster, Priestley, Kelvin, and the Curies. The pyroelectric effect is the physical basis for a wide range of radiation detectors, most notably for infrared radiation (IR). The first description of a pyroelectric infrared detector (PIRD) was by Yeou Ta[4] who, in 1938, described the use of a thin piece of tourmaline to detect IR emitted by warm bodies. The radiation was allowed to warm the tourmaline, and the resulting pyroelectric current was detected using a sensitive galvanometer. In 1939, Leon Sivian filed a U.S. patent (published 1942[5]), which described a very similar device.

The basic structure of a simple single element pyroelectric radiation sensor is shown in the schematic diagram in Fig. 2(a), with a photograph of a practical device in Fig. 2(b). It consists of a thin chip of a pyroelectric material (the "element"), sometimes coated with a layer designed to absorb the radiation of-interest, placed inside a hermetically sealed package (usually a transistor "header" of the TO type), and accompanied by an amplifier plus its passive components. The pyroelectric element is usually made as thin as possible (typically in the range of 30—50 μm thickness for a bulk material) and fixed to a mount designed to minimize thermal conduction to the environment. Both design aspects are intended to maximize the change in temperature due to the absorbed energy. One major advantage of these sensors is that they are sensitive only to the amount of energy absorbed by the element and not to its wavelength, unlike photon detectors based on semiconductors. They have been used to detect radiation from the microwave[6] and millimeter[7] wave regions of the electromagnetic spectrum right out to x rays,[8] but their use to detect IR radiation at wavelengths longer than a few microns is a particularly important application. In this region, semiconducting detectors need to be cooled for best efficiency, often to temperatures below 100 K. IR in the range of 3–5 μm is interesting for, e.g., gas analysis and flame detection through the detection of the emission from the hot CO/CO_2 gases released by the fire. Longer wavelengths in the range of 8–12 μm are used for the detection of warm targets such as people, as objects around 310 K emit most of their thermal radiation in this waveband. Note also that the atmosphere shows high transmission in these two spectral bands.[9] A transparent window on the front of the package is

© Author(s) 2023

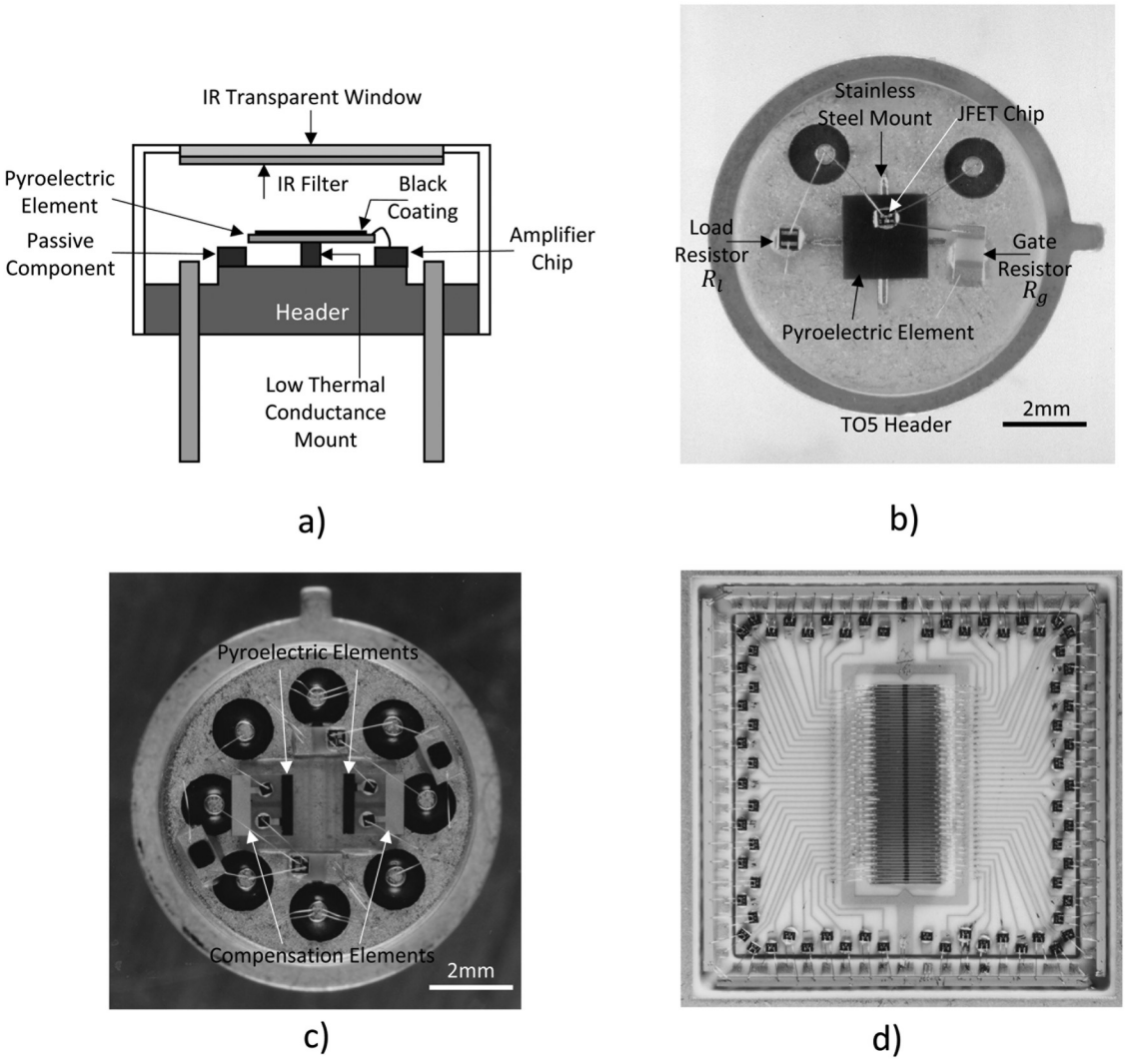

FIG. 2. Illustrating some different types of pyroelectric infrared detectors (PIRDs). (a) A schematic diagram of a single-element PIRD showing the different components; images of (b) a PIRD using a 2 × 2 mm $LiTaO_3$ element with an in-package JFET amplifier and resistors; (c) a PIRD consisting of two compensated active elements, each sensitive element being 0.3 × 1.5 mm and the compensation elements 0.45 × 1.5 mm in size; (d) a 1D linear array, each element being 50 × 150 μm with a compensation element 50 × 650 μm in size.

used as both an environmental and electromagnetic seal and to filter the wavelengths of radiation that can reach the detector element through a combination of the intrinsic optical properties of the window and, frequently, an optical coating. It can be seen from Eq. (2) that i_p is proportional to the rate of change of the element temperature with time, which means that PIRDs are not sensitive to the unchanging fluxes of radiation. This can be advantageous in many applications, as they will only respond to changes in the environment, such as an intruder moving into the field-of-view of the sensor. However, it also means that if a PIRD is required to sense a static scene, then provision must be made to modulate the incident IR, usually with a rotating[10] or vibrating[11,12] mechanical "chopper." Many different types of PIRDs have been developed and applied, including devices with "compensation" elements [illustrated in Fig. 2(c)], which help to minimize interference from effects such as ambient temperature changes and mechanical vibrations, one-dimensional arrays [see an example in Fig. 2(d)] for use in applications such as IR spectroscopy, and two-dimensional arrays for applications in thermal imaging.

PIRDs and PIRD arrays[13,14] are now widely used and have been demonstrated in many applications such as intruder sensors,[15] automatic/remote light switches,[16] environmental monitors,[17] flame detectors,[18] medical instrumentation such as

© Author(s) 2023

capnography,[19] fall detection in the care sector,[20] retail footfall counting,[21] and thermal imaging.[22] PIRD had a market of ca. U.S.$50 million in 2020, expected to reach U.S.$68 million by 2025, or about 10% of the total infrared detector market.[23] This article will analyze the physics and engineering of these devices and take a critical perspective on the current state of research into the pyroelectric materials used to make them.

II. PYROELECTRIC INFRARED DETECTOR PHYSICS

When considering the physics of a PIRD, it is essential to look at both the electrical and thermal structures of the device. Figure 3(a) shows the basic electrical configuration. The pyroelectric detector element appears as a capacitor of area A and thickness d in parallel with a current generator, which represents i_p given by

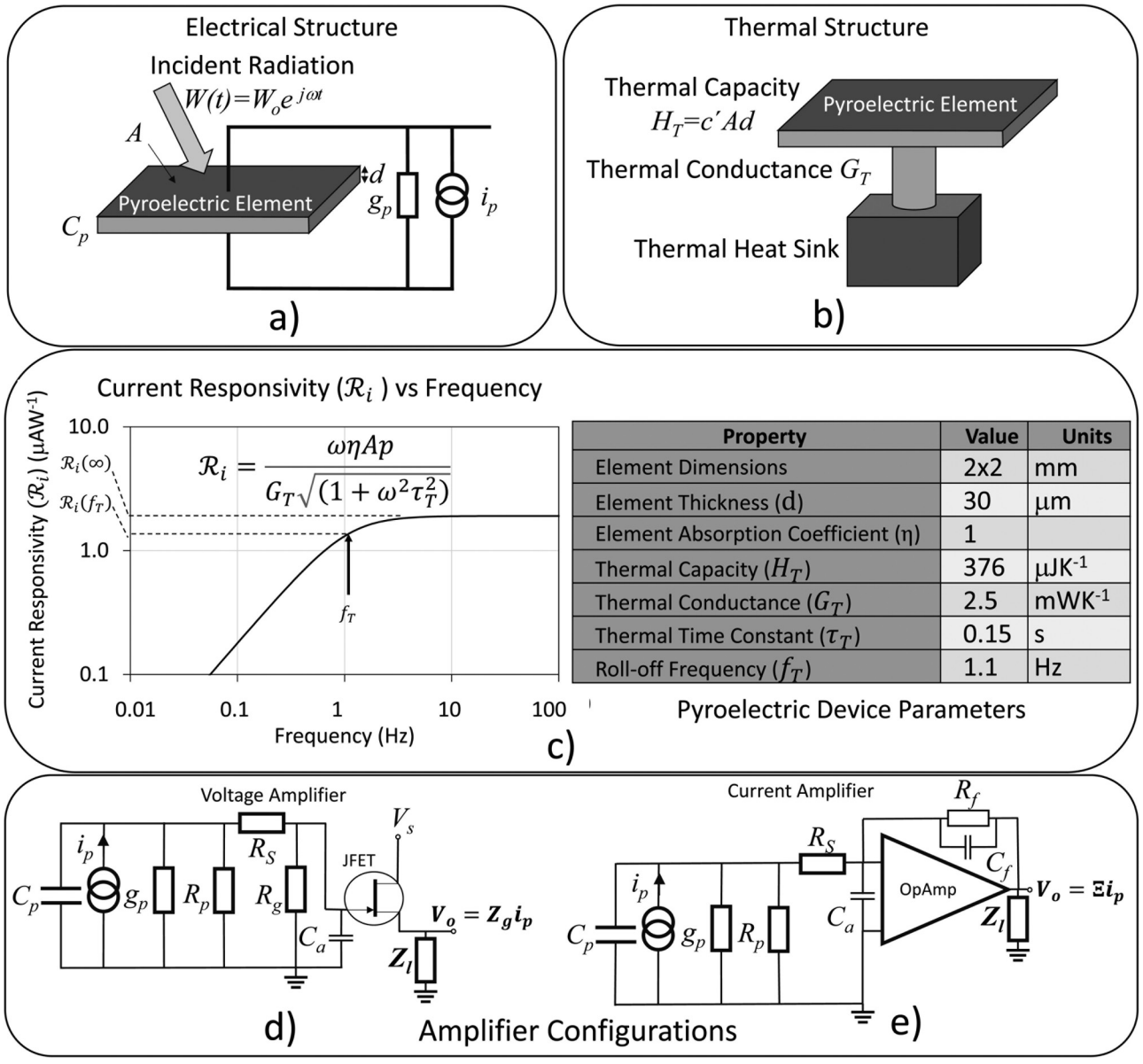

Property	Value	Units
Element Dimensions	2x2	mm
Element Thickness (d)	30	μm
Element Absorption Coefficient (η)	1	
Thermal Capacity (H_T)	376	μJK^{-1}
Thermal Conductance (G_T)	2.5	mWK^{-1}
Thermal Time Constant (τ_T)	0.15	s
Roll-off Frequency (f_T)	1.1	Hz

FIG. 3. Thermal and electrical structures of a simple pyroelectric infrared detector: (a) the electrical structure and (b) the thermal structure of the device; the device configurations using (c) a voltage amplifier and (d) a current amplifier.

© Author(s) 2023

Eq. (2). The capacitance C_p of the pyroelectric element is given by

$$C_p = \frac{A\,\varepsilon_p\,\varepsilon_o}{d}, \tag{3}$$

where ε_p is the dielectric permittivity of the pyroelectric material and ε_o is the permittivity of free space. The element also has an electrical resistance, R_p, given by

$$R_p = \frac{\rho_p d}{A}, \tag{4}$$

where ρ_p is the DC resistivity of the pyroelectric material. Pyroelectric devices only respond to changes in the temperature of the pyroelectric element, so they are inherently AC in operation and it is, therefore, necessary to consider the AC electrical conductance, g_p, of the pyroelectric element, which appears in parallel with C_p and R_p,

$$g_p = \omega C_p \tan\delta_p, \tag{5}$$

where $\tan\delta_p$ is the dielectric loss tangent of the pyroelectric material.

The thermal structure of the element (in this simple case) is represented as thermal capacitance $H_T = c' Ad$ (where c' represents the volume specific heat of the pyroelectric material), which is in series with a thermal conductance G_T, as shown in Fig. 3(b). G_T is determined by the design of the device and the materials used to make it. Assume that the element is illuminated by sinusoidally modulated radiation with a power $W(t) = W_o e^{j\omega t}$, where W_o is the amplitude of the incident radiation, ω is the angular frequency, t is the time, and $j = \sqrt{-1}$. In this simple case, the thermal response can be calculated by using the following heat flow equation:[24,25]

$$W(t) = H_T \frac{d\theta}{dt} + G_T \theta. \tag{6}$$

This has the solution

$$\theta = \frac{\eta W_o}{G_T + j\omega H_T} e^{j\omega t}, \tag{7}$$

where η is the element absorption coefficient or the fraction of incident radiation power absorbed by the detector. In a practical detector, η should be made as close to unity as possible within reasonable manufacturing cost constraints. There are various strategies that can be used to achieve this, including the use of external absorbing coatings such as gold[26] or platinum[27,28] blacks, or carbon nanotubes,[29] or simply by using the intrinsic absorption of the pyroelectric material. In the latter case, the pyroelectric material should be coated with a thin electrode designed to have the same electric impedance as free space (377 Ω/square).[30] Note that, in any practical detector, the IR transparent window [see Fig. 2(a)] will have a transmittance <100%. This can be accounted for in the model by an appropriate adjustment of η, which, then, would combine both element absorption and window transmission.

$\boldsymbol{i_p}$ can be derived using Eq. (2) as follows:

$$\boldsymbol{i_p} = \frac{j\,W_o \omega \eta A p}{G_T(1 + j\tau_T \omega)}, \tag{8}$$

where τ_T is the thermal time constant of the detector element, described by $\tau_T = H_T/G_T$ (note that the bold type, e.g., $\boldsymbol{i_p}$, is used to indicate a complex quantity). The current responsivity $\boldsymbol{\mathcal{R}_i}$ is defined as the pyroelectric current per watt of input power,

$$\boldsymbol{\mathcal{R}_i} = \boldsymbol{i_p}/W_o = \frac{j\,\omega \eta A p}{G_T(1 + j\omega\tau_T)}. \tag{9}$$

The magnitude of $\boldsymbol{\mathcal{R}_i}$ is denoted by $\mathcal{R}_i$,

$$\mathcal{R}_i = \frac{i_p}{W_o} = \frac{\omega \eta A p}{G_T\sqrt{(1 + \omega^2 \tau_T^2)}}. \tag{10}$$

The current responsivity for a typical single-element pyroelectric detector is shown in Fig. 3(c). The device parameters used to calculate this are indicated in the accompanying table within the figure. The material properties are those for lithium tantalate ($LiTaO_3$—LTO), a pyroelectric material widely used in commercial PIRDs, taken from Schossig *et al.*[31] These properties are listed in Table I and will be discussed in more detail below. The device parameters (linear dimensions and thermal properties) are typical of those for commercial devices. It can be seen from the figure that the voltage responsivity is constant at high frequencies, with a value $\mathcal{R}_i(\infty) = \{\eta A p/G_T \tau_T\}$. $\mathcal{R}_i$ rolls off as $1/f$ below $f_T = 1/(2\pi\tau_T)$. At this frequency, $\mathcal{R}_i = \mathcal{R}_i(f_T) = \mathcal{R}_i(\infty)/\sqrt{2}$. We can define a normalized complex current responsivity as

$$\boldsymbol{\Gamma_i} = \frac{\boldsymbol{\mathcal{R}_i}}{\mathcal{R}_i(\infty)} = \frac{j\,\tau_T}{(1 + j\omega\tau_T)}. \tag{11}$$

The pyroelectric current is presented to an electrical impedance $\boldsymbol{Z_g}$, consisting of a parallel combination of the following circuit elements: a gate resistor, R_g, R_p, g_p [see Eq. (5)], the element capacitance, C_p, and the amplifier capacitance, C_a. $\boldsymbol{Z_g}$ is given by

$$\begin{aligned}\boldsymbol{Z_g} &= \left\{R_g^{-1} + R_p^{-1} + g_p + j\omega(C_p + C_a)\right\}^{-1} \\ &= \left\{R_g^{-1} + R_p^{-1} + \omega C_p \tan\delta_p + j\omega(C_p + C_a)\right\}^{-1}.\end{aligned} \tag{12}$$

The resulting output voltage is amplified with a unity-gain, high input impedance voltage amplifier, such as the source follower junction field effect transistor (JFET) as indicated in Fig. 3(c), to produce an output voltage $\boldsymbol{V_o}$,

$$\boldsymbol{V_o} = \boldsymbol{Z_g}\boldsymbol{i_p}. \tag{13}$$

Alternatively, it can be passed to a current amplifier, such as an operational amplifier (OpAmp) with a feedback network consisting of a feedback capacitor C_f and feedback resistor R_f, as

© Author(s) 2023

TABLE I. Properties derived from the literature of some ferroelectric materials that have been considered for use in PIRDs. All properties measured at 25 °C.

Material Name	Material code	Type	p	Dielectric properties		Freq	c'	T_d	F_i	F_V	F_D	DC resistivity (ρ_o)	Reference
			$\mu Cm^{-2} K^{-1}$	ε	$tan\delta$	Hz	$MJm^{-3} K^{-1}$	°C	$pm\ V^{-1}$	m^2C^{-1}	$mPa^{-½}$	GΩm	
$LiTaO_3$	LTO	Crystal	176	43.3	0.00015 to 0.001	1000	3.13	603.5	56	0.15	234.5	1.15×10^4	Refs. 31,55
Deuterated Triglycine Sulfate	DTGS	Crystal	264	26.3	0.014	1000	2.38	61	111	0.48	61.4	2.31 $x10^6$	Refs. 56–60
Poly(vinylidenefluoride-trifluoroethylene) Copolymer	P(70VDF-30TrFE)	Polymer	33	10.7	0.0155	1000	2.3	121	14	0.151	11.8	3.91×10^5	Refs. 61–66
$Pb(Zr_{0.25}Ti_{0.75})O_3$	PZT25/75	Thin Film	260	380	0.01	30	2.7	410	96	0.03	16.6	3000	Ref. 67
$Pb_{(1-x)}Ca_x[(Co_{½}W_{½})_yTi_{1-y}]O_3$; x = 0.27, y = 0.04; 1%Mn	PCT:Mn	Ceramic	385	200	0.011	1000	2.55	270	151	0.09	34.2	8	Refs. 68–71
$Pb[Zr_{1-x-y}(Fe_{½}Nb_{½})_xTi_y]_{1-z}U_zO_3$; x = 0.2,y = 0.02,z = 0.005	PZFNTU	Ceramic	410	284	0.0027	1592	2.67	230	154	0.06	58.9	8	Refs. 14,72–74
				300	0.0094	80				0.06	30.7		
				300	0.014	33				0.06	25.2		
$Pb[(Mg_{⅓}Nb_{⅔})_xTi_{1-x}]O_3$; x = 0.72 (111)	PMNT73/27 (111)	Crystal	1280	600	0.003	100	2.64	103	485	0.091	121.5	–	Refs. 75–78
$xPb(In_{½}Nb_{½})O_3-yPb[(Mg_{⅓}Nb_{⅔})_xTi_{1-x}]O_3$-(1−x−y)PbTiO3; x = 0.41,y = 0.17 (001)	PIMNT41/17/42 (001)	Crystal	570	487	0.003	50	2.64	253	216	0.050	60.0	–	Refs. 77–79
$xPb(In_{½}Nb_{½})O_3-yPb[(Mg_{⅓}Nb_{⅔})_xTi_{1-x}]O_3$-(1−x−y)PbTiO3-Mn; x = 0.23,y = 47 (001)	PIMNT:Mn23/47/30 (111)	Crystal	770	570	0.0003	1,000	2.64	115	292	0.058	237.0	60	Refs. 77,78,80
0.97(0.99 $Na_{½}Bi_{½}TiO_3$-0.01$BiAlO_3$)-0.03$K_{½}Na_{½}NbO_3$	NBT-BA-KNN	Ceramic	370	514	0.029	1000	2.8	118	132	0.029	11.5	–	Ref. 81
				551	0.03	20				0.027	10.9		
$91.5Na_{½}Bi_{½}TiO_3$–$8.5K_{½}Bi_{½}TiO_3$ <111>	91.5NBT–8.5KBT <111>	Crystal	563	350	0.026	100	3.12	153	180	0.058	20.1	–	Ref. 82
93.6 $Na_{½}Bi_{½}TiO_3$–5.4$BaTiO_3$:0.14Mn <111>	93.6NBT–5.4KBT:Mn <111>	Crystal	588	279	0.0188	100	2.89	120	203	0.082	29.9	–	Ref. 83

© Author(s) 2023

shown in Fig. 3(d), in which case

$$V_o = \Xi i_p, \tag{14}$$

where Ξ is the current-to-voltage transfer function for the amplifier (in both cases, the amplifier load is represented by a load impedance Z_l). Both types of amplifiers are used in commercial PIRDs. The output voltages defined by Eqs. (13) and (14) can be normalized to give voltage responsivities ($\mathcal{R}_V$, in units of V W^{-1}) by dividing through the relevant expressions by W_o.

There are two main performance-defining parameters used for PIRDs. The first is the noise equivalent power, or *NEP*, defined[32] as the input RMS radiation power required to give a signal equal to the RMS noise in a defined bandwidth, ΔV_N. *NEP* is defined in units of W Hz$^{-½}$,

$$NEP = \frac{\Delta V_N}{\mathcal{R}_V}. \tag{15}$$

The second is the specific detectivity,[32] or D^*, defined as the inverse of the NEP, normalized to the square root of the PIRD element area,

$$D^* = \frac{\sqrt{A}}{NEP}. \tag{16}$$

D^* is generally expressed in units of cm Hz^{½} W^{-1}.

A. Voltage amplifier responsivity

In the case of PIRDs using voltage amplifiers, the voltage responsivity $\mathcal{R}_V$ can be computed from Eq. (13) as

$$\mathcal{R}_V = \frac{1}{(R_g^{-1} + R_p^{-1} + \omega C_p tan\delta_p + j\omega(C_p + C_a))} \cdot \frac{j\omega\eta Ap}{G_T(1 + j\tau_T\omega)} \tag{17}$$

If $\omega C_p tan\delta_p$ and R_p^{-1} are small in comparison with R_g^{-1} and $\omega(C_p + C_a)$, then the magnitude of $\mathcal{R}_V$ is given by

$$\mathcal{R}_V = \frac{\omega\eta R_g Ap}{G_T\sqrt{(1 + \tau_T^2\omega^2)}\sqrt{(1 + \tau_{EV}^2\omega^2)}}, \tag{18}$$

where $\tau_{EV} = R_g(C_p + C_a)$ is the electrical time constant for this type of amplifier.

In almost all treatments of PIRD physics, C_p and $tan\delta_p$ are taken as being frequency-independent, but this is very rarely the case for ferroelectric materials, which is a point discussed in greater detail in the next section.

Equation (18) is a very well-known expression,[13,25,33] which is plotted in Fig. 4 for an LTO detector with the device parameters listed in Figs. 3(c) and 3(a). JFET has an input capacitance of $C_a = 7$ pF. C_a is much smaller than the element capacitance C_p in this case, which is around 50 pF. $\mathcal{R}_V$ maximizes with a value of

$$\mathcal{R}_V(Max) = \frac{\eta R_g Ap}{G_T(\tau_T + \tau_{EV})}, \tag{19}$$

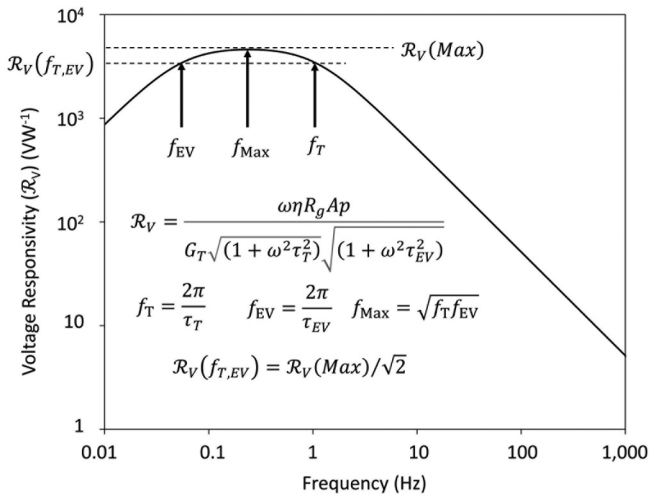

FIG. 4. The voltage responsivity R_V of a $LiTaO_3$ PIRD with the characteristics shown in Fig. 3(c).

at a frequency $f_{Max} = \sqrt{f_T f_E}$, where $f_{EV} = 1/(2\pi\tau_{EV})$. At frequencies f_T and f_{EV}, $\mathcal{R}_V$ has a value $\mathcal{R}_V(f_{T,EV}) = \sqrt{2}.\mathcal{R}_V(Max)$. The voltage responsivity for this modeled device would be typical for a high-end commercial PIRD and agrees well with the published datasheet values for, e.g., an InfraTec 316 device. An important point to take from this figure is that the response of a PIRD maximizes in the low-Hz to sub-Hz range, dropping off rapidly (as $1/f$) both above and below the turn-over frequencies defined by f_T and f_{EV}. This makes them ideal for use in applications where a good response at low frequencies is required, such as intruder sensing and flame detection. The zero response at DC means that they are insensitive to very slow changes in ambient temperature, and they do not "see" an unchanging background scene but only respond to the stimuli of interest. They can also be engineered by changing G_T and R_g to give a flat frequency response over a very wide frequency range (up to GHz if needed), but this is at the expense of absolute responsivity, so they are good in applications where there is plenty of signal available to detect, such as for fast (sub-microsecond to picosecond) laser pulse characterization.[34,35]

B. Voltage amplifier noise

The RMS current noise sources in a PIRD can be summarized as follows:[36,37]

Input thermal noise, $N_{\theta i}$:

$$N_{\theta i} = \sqrt{(4k\Theta^2 G_T)}.\mathcal{R}_i. \tag{20}$$

Input amplifier current noise (sometimes called "shot" noise), N_{iai}:

$$N_{iai} = \sqrt{2qi_{leak}} \text{ where } q = \text{charge on electron and } i_{leak} = \text{input leakage current of amplifier.} \tag{21}$$

© Author(s) 2023

N_{ia} and/or i_{leak} can be specified on the amplifier datasheet. N_{ia} is usually defined in fA $Hz^{-½}$. In addition, values for the low noise JFETs used in PIRDs are in the range of 0.2–0.3 fA $Hz^{-½}$.

Input resistor Johnson noise, N_{Rgi}:

$$N_{Rgi} = \sqrt{(4k\Theta/R_g)}. \tag{22}$$

Input pyroelectric chip DC resistance Johnson noise, N_{Rpi}:

$$N_{Rpi} = \sqrt{(4k\Theta/R_p)}. \tag{23}$$

Input pyroelectric chip AC resistance ($tan\delta$) Johnson noise, N_{Ji}:

$$N_{Ji} = \sqrt{(4k\Theta\omega C_p \tan\delta_p)}. \tag{24}$$

Determining an appropriate value of $\tan\delta_p$ to use in Eq. (24) can be problematic. $tan\delta_p$ has been shown to have three components:[31]

- $tan\delta_i$: Loss intrinsic to the pyroelectric material and dependent on such factors as intrinsic bulk and surface defects together with species such as mobile charge carriers.
- $tan\delta_{RS}$: Loss due to a resistance R_S in series with C_p—see Figs. 3(d) and 3(e), such as the surface and contact resistances of the electrodes on the pyroelectric. This can be a significant effect and is dependent on the quality of sample-preparation.
- $tan\delta_\theta$: Loss caused by electrothermal coupling, as discussed by Nye[38] in his discussion of the difference between permittivities measured under isothermal and adiabatic conditions.

The effects of electrothermal coupling have been discussed by Stokowski,[39] Samoilov and Shchedrina,[40,41] and Neumann and Möhling,[42] and it can be shown that

$$\tan\delta_\theta = k_\theta^2 \frac{\omega\,\tau_T}{(1+(\omega\tau_T)^2)}, \tag{25}$$

where k_θ is the electrothermal coupling factor defined by

$$k_\theta^2 = \frac{p^2\Theta}{c'\varepsilon\varepsilon_o}. \tag{26}$$

The magnitude of $tan\delta_\theta$ can be significant, and in some cases, it can dominate the intrinsic loss, especially if $tan\delta_i$ is small. For example, Stokowski[39] showed that in measurements on a LTO crystal, at some frequencies, a freely suspended sample gave a $tan\delta_p$ several times lower than a sample heat-sunk onto a copper block, concluding that $tan\delta_i$ in this material was about 7×10^{-5}. On the other hand, Schossig *et al.*[31] concluded from measurements on crystal plates ranging from 100 μm down to 0.55 μm in thickness that the intrinsic loss for LTO was 1.5×10^{-4} for a bulk material, rising inversely proportional to thickness for thicknesses below about 10 μm to a value of about 2.5×10^{-3} at thicknesses below 0.8 μm due to an increase in surface imperfections. The recommendation of these authors is that the intrinsic loss can be measured on bulk materials at frequencies of about 1 kHz and at ca. 200 Hz for thin films below 2 μm thickness. However, few authors take account of electrothermal effects when reporting dielectric loss measurements on pyroelectric materials, and, given the impossibility of knowing the thermal conditions under which such measurements are taken, it is very hard to conclude what the true value of $tan\delta_i$ may be for any given material. Stokowski[39] has pointed out that a measurement of $tan\delta_p$ as a function of frequency for any practical PIRD element gives all that is needed for a prediction of N_{Ji} in that device, but this does not help an engineer trying to predict how a new material will behave in a different device design simply based on the published properties of the material concerned. A further complication comes from the fact that $tan\delta_i$ is usually frequency dependent, sometimes strongly so in the frequency range of greatest interest for PIRDs (0.1–100 Hz).[43] This frequency dependence needs to be taken account of in any model for N_{Ji}. Unfortunately, many papers that discuss pyroelectric materials do not report the dielectric properties as functions of frequency, and often the values quoted for permittivity and loss will have been determined at a single frequency (often at ca. 1 kHz), which is well above the frequencies at which most pyroelectric devices are used. While one can take this as an estimate of $tan\delta_i$ and use this in the responsivity and noise equations, there is no guarantee that this will give an accurate prediction for device performance.

The excess loss due to the resistance R_S of the surface electrodes can be shown to be

$$\tan\delta_{RS} = R_S\left\{\frac{A}{d}\sigma(\omega)\tan\delta_i + \omega C_p\right\}, \tag{27}$$

where $\sigma(\omega)$ is the AC conductivity of the pyroelectric material, which is discussed further below.

In addition, we need to take account of the input-referred voltage noise of the amplifier, $\overline{e_n}(f)$. This has a constant value, $\overline{e_n}$, at high frequencies, and a frequency dependence such that $\overline{e_n}(f)^2 \propto 1/f$ at frequencies below a value f_o (an "elbow" frequency).[44,45] In the general case, $\overline{e_n}(f)$ can be described by an equation of the following form:[46]

$$\overline{e_n}(f) = \overline{e_n}\left(1+\left(\frac{f_o}{f^{If}}\right)\right)^{0.5}, \tag{28}$$

where f_o is an "elbow" frequency and If is an "inflection factor" (typically around 1.3).

Figure S1 in the supplementary material shows $\overline{e_n}(f)$ for two JFET devices, one taken from the datasheet of a PIRD manufacturer (InfraTec) as their standard device JFET[47] and one from the datasheet for a low noise device (JFE150)[48] manufactured by Texas Instruments. Also shown are models used to describe them as functions of frequency. At low frequencies, the InfraTec JFET gives a frequency dependence $\overline{e_n}(f) \propto \left(\frac{f_o}{f}\right)^{0.175}$ with $\overline{e_n} = 8\,\text{nVHz}^{-}1/2$ (at 1 kHz), while the JFE150 gives $\overline{e_n}(f) \propto \left(\frac{f_o}{f}\right)^{0.62}$ with $\overline{e_n} = 0.93\,\text{nVHz}^{-}1/2$. The amplifier voltage noise may be

© Author(s) 2023

represented by an input current noise,

$$N_{Vi} = \frac{\overline{e_n}(f)}{\boldsymbol{Z_i}} \text{ where } \boldsymbol{Z_i} = \left\{R_g^{-1} + R_p^{-1} + \omega C_p \tan\delta_p + j\omega C_p\right\}^{-1}. \tag{29}$$

To find the corresponding output RMS voltage noises in an amplifier as shown in Fig. 3(d), the input current noises should be multiplied by the complex impedance $\boldsymbol{Z_g}$ from Eq. (12). With the low noise amplifiers currently available, voltage noise is rarely a problem for PIRDs in the low-medium frequency range.

Figure 5 plots the magnitudes of the different noise sources, as well as the total noise for a model device consisting of a 2 × 2 mm area, 30 μm thick LTO element feeding into a low noise JFET such as a TI JFE150 and employing a 50 GΩ gate bias resistor. The values of τ_E and τ_T are 2.9 s and 150 ms, respectively. The relevant physical properties of LTO are given in Table I. The relative magnitudes of the predicted noise sources are typical for those reported for this type of device.[47] The important things to note about this are as follows:

- The total noise below about 100 Hz is dominated by the Johnson noise from the gate bias resistor.
- The "tan delta" noise from the pyroelectric chip only becomes significant above about 100 Hz in this example. The frequency at which this noise source will dominate will depend on the precise design of the device and the magnitude of $tan\delta_i$ for the pyroelectric material being used. This point is discussed further below.
- The voltage noise from the JFET is not important in this frequency range. Even for JFETs with somewhat higher voltage noise, this noise source is only likely to become important at frequencies above 1 kHz.
- The current noise of the JFET hardly contributes to the total noise, even at low frequencies, and the thermal noise is unimportant.

These are important considerations when it comes to judging the likely usefulness of a given pyroelectric material. For completeness, Fig. 6(a) plots the predicted NEP and Fig. 6(b) the D^* for a device with the same design. These are also typical for this type of device.[47]

A further practical consideration when using pyroelectric devices is the fact that all polar dielectrics are piezoelectric, sometimes strongly so. This means that a PIRD can generate significant unwanted noise known as piezoelectric "microphony" when operated in a vibration-rich environment, such as when used close to vibrating machinery. There are two piezoelectric modes, which are important in determining the strength of this response.[28] These are the following:

- The "thickness" mode (TM), driven via the piezoelectric d_{33} coefficient, whereby accelerations perpendicular to the plane of the detector element produce a microphonic response via self-loading.
- The "lateral" mode (LM) whereby acceleration-induced mechanical strains in the system are coupled via the PIRD package to induce lateral strains in the plane of the detector element and these couple via the piezoelectric d_{31} coefficient.

In general, the LM is a more significant noise source than the TM but can be reduced dramatically through good mechanical design of the element mounting[49] and the system in general[28] to minimize lateral stresses on the pyroelectric element. Both TM and LM can be much reduced through including a "compensation" element—an unilluminated pyroelectric element included in the package and wired either in series or in parallel with the detector element. This acts to provide the common-mode rejection of unwanted signals such as microphony and ambient temperature changes. To be effective in reducing microphony, the compensation

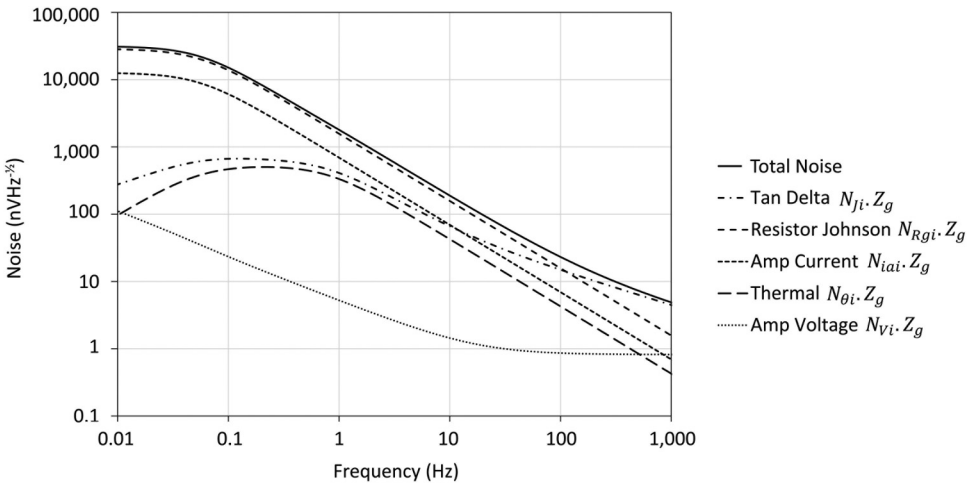

FIG. 5. The different magnitudes of noise sources as functions of frequency in a typical PIRD using a 2 × 2 mm area, 30 μm thick $LiTaO_3$ pyroelectric element and a low noise JFET amplifier (see the text for a full description of the parameters used).

© Author(s) 2023

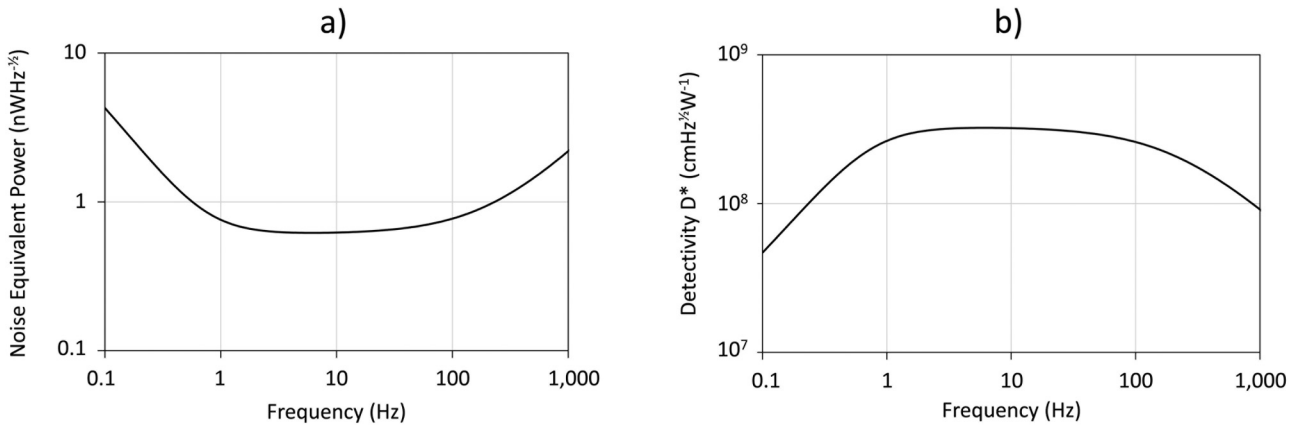

FIG. 6. (a) Noise equivalent power (NEP) and (b) detectivity D^* as functions of frequency for a typical PIRD using a 2 × 2 mm area, 30 μm thick $LiTaO_3$ pyroelectric element and a low noise JFET amplifier (see the text for a full description of the parameters used).

element needs to be mounted in a mechanical environment that is closely similar to the detector. The inclusion of a compensation element generally comes at a cost in the signal-to-noise ratio, the level of which depends on the size of the compensation element but would typically be about a factor of $\sqrt{2}$. In general, a good device design can radically reduce microphony and so this, and the use of compensation, will not be considered further here.

C. Current amplifier responsivity

The ready-availability at low cost of high input impedance, low-noise operational amplifiers, which can be operated in a current-amplifier mode as shown in Fig. 3(d), bring with it a different approach to the amplification of the pyroelectric current given in Eq. (8). This is governed by a different set of equations from the voltage amplifier.

The responsivity of the current amplifier configuration shown in Fig. 3(e) can be modeled using the well-known theories describing the use of an OpAmp as a current amplifier.[50,51] Provided the output resistance of the OpAmp is small, the current-to-voltage transfer function in Eq. (14) is given by

$$\Xi = \frac{\boldsymbol{Z_f}}{(1 + (\boldsymbol{A_{OL}\beta})^{-1})}, \tag{30}$$

where $\boldsymbol{Z_f}$ is the impedance of the feedback RC network,

$$\boldsymbol{Z_f} = \frac{R_f}{(1 + j\omega R_f C_f)} = \frac{R_f}{(1 + j\omega\tau_f)} \text{ and } \tau_f = R_f C_f, \tag{31}$$

and β is a feedback factor, such that $\boldsymbol{\beta} = \frac{\boldsymbol{Z_f}}{(\boldsymbol{Z_f}+\boldsymbol{Z_i})}$.

$\boldsymbol{Z_i}$ is the input impedance presented to the amplifier,

$$\boldsymbol{Z_i} = \frac{R_{in}}{(1 + j\omega R_{in} C_{in})} = \frac{R_{in}}{(1 + j\omega\tau_{in})}, \tag{32}$$

and $R_{in} = (\omega C_p tan\delta + R_p^{-1} + R_a^{-1})^{-1}$, $C_{in} = (C_p + C_a)$, $\tau_{in} = R_{in}C_{in}$.

Note that here, it is assumed that C_p and $tan\delta$ are frequency independent and that R_p is determined by the DC resistivity of the pyroelectric material.

The OpAmp parameters are

$\boldsymbol{A_{OL}}$ = Open loop gain.
R_a = Input resistance.
C_a = Input capacitance.

$\boldsymbol{A_{OL}}$ rolls off at a rate of 20 dB/decade above a frequency f_p. $\boldsymbol{A_{OL}}$ can be modeled as

$$\boldsymbol{A_{OL}} = \frac{A_{DC}}{\left(1 + j\frac{f}{f_p}\right)} \tag{33}$$

where A_{DC} is the amplifier gain at low frequencies.

Equation (30) reduces to

$$\Xi = \frac{\boldsymbol{A_{OL}Z_f Z_i}}{\boldsymbol{Z_i}(1 + \boldsymbol{A_{OL}}) + \boldsymbol{Z_f}}. \tag{34}$$

Figure 7(a) shows the voltage responsivity of a 2 × 2 mm area, 30 μm thick LTO pyroelectric element as described in Fig. 3(c), connected to a low noise OpAmp with characteristics similar to that of "OpAmp 2" described by InfraTec in their "Pyroelectric Library."[47] The feedback network in this case was set with $R_f = 50\,G\Omega$ and $C_f = 0.2\,pF$. The responsivity of a similar element feeding into a JFET voltage amplifier [see Fig. 3(d)] with $R_g = 50\,G\Omega$ is also plotted on the figure. Some important differences are immediately apparent. The built-in gain of the OpAmp produces a peak voltage responsivity that is more than an order-of-magnitude greater for the current-amplified relative to the voltage-amplified device. Note that while the two "turnover" frequencies for the voltage-amplified device are f_T and f_{EV} (defined, respectively, by the thermal and electrical time constants, τ_T and τ_{EV}—see above), the corresponding frequencies for the current-amplified device are f_T and f_{Ei}, where $f_{Ei} = 1/(2\pi\tau_f)$

© Author(s) 2023

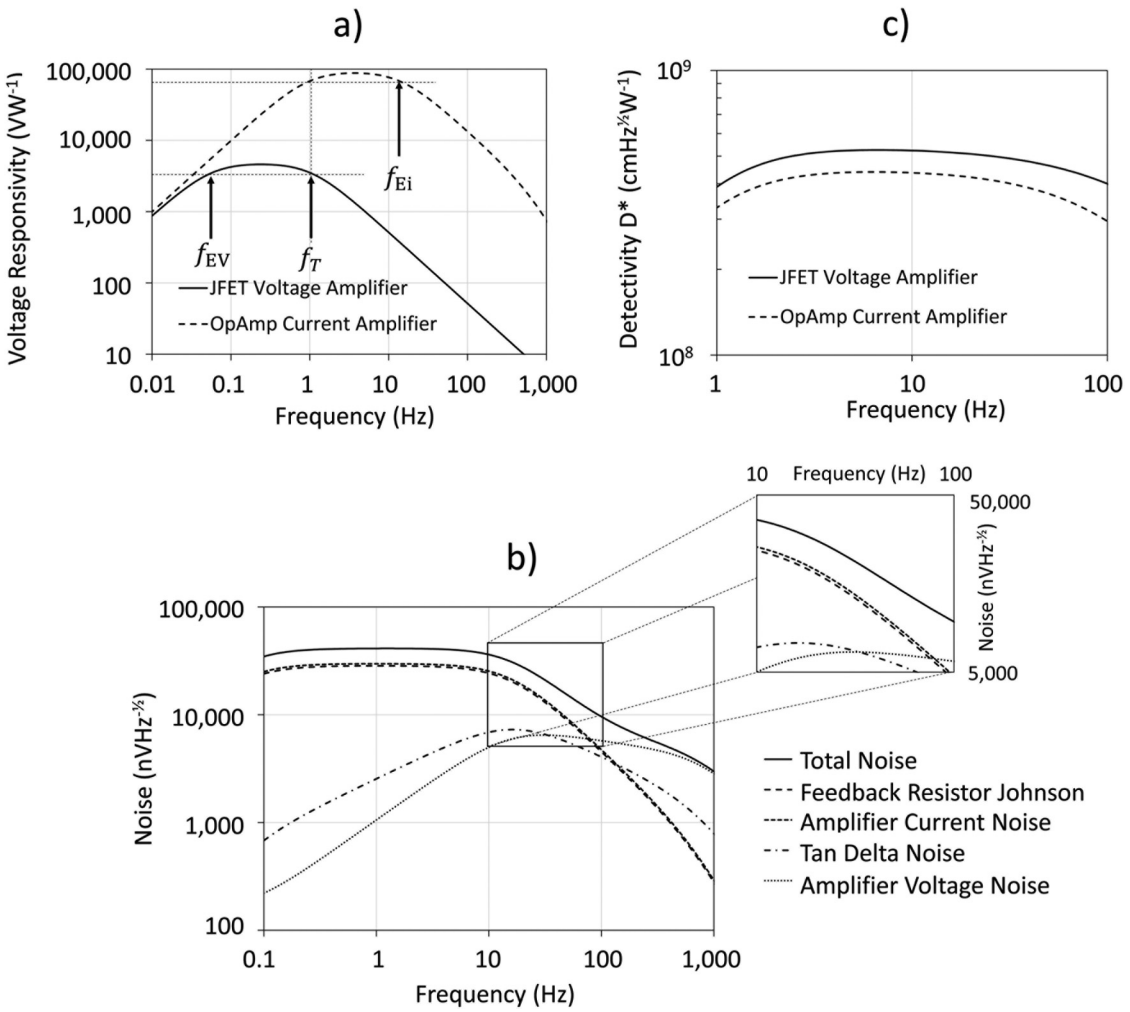

FIG. 7. (a) Voltage responsivity R_V vs frequency for a PIRD using a 2 × 2 mm area, 30 μm thick $LiTaO_3$ pyroelectric element and a low noise OpAmp in the current mode with a feedback network consisting of a 50 GΩ resistor and 0.2 pF capacitor in parallel. For comparison, R_V for a similar device using a low noise JFET voltage amplifier and 50 GΩ gate resistor is presented on the same axes. (b) The different magnitudes of the principal noise sources vs frequency for the current-amplified PIRD discussed in the text. The inset shows a magnified section of the graph from 10 to 100 Hz, to indicate that in this case, the curves for the amplifier current noise and feedback resistor Johnson noise lie almost on top of one another. (c) Detectivity D^* vs frequency for the devices discussed in (a).

and τ_f is the electrical time constant of the feedback network defined in Eq. (31). As $C_f \ll C_p$ for this size of element, then $\tau_f \ll \tau_{EV}$, so the voltage responsivity for the current-amplified device turns over at a significantly higher frequency than that for the voltage-amplified device. The higher voltage responsivity and different frequency response characteristics may be useful to an end-user in some applications.

D. Current amplifier noise

The input current noises described by Eqs. (20)–(24), including the input-referred current noise of the amplifier, must be multiplied by a current noise to voltage noise transfer function Ξ_{Ni}, which is given by

$$\Xi_{Ni} = \frac{Z_f Z_{Total} A_{OL}}{Z_i(1 + A_{OL}) + Z_f}, \tag{35}$$

where

$$Z_{Total} = \frac{R_{Total}}{(1 + j\omega R_{Total} C_{Total})} = \frac{R_{Total}}{(1 + j\omega \tau_{Total})}, \tag{36}$$

© Author(s) 2023

and

$$R_{Total} = (\omega C_D tan\delta_p + R_p^{-1} + R_a^{-1} + R_f^{-1})^{-1},$$

$$C_{Total} = C_p + C_a + C_f \text{ and } \tau_{Total} = C_{Total} R_{Total}.$$

Note that the input-resistor Johnson current noise N_{Rgi} defined in Eq. (22) must be replaced by the feedback resistor Johnson noise N_{Rfi},

$$N_{Rfi} = \sqrt{(4k\Theta/R_f)}. \tag{37}$$

The input-referred voltage noise for the OpAmp must be multiplied by a different transfer function Ξ_{NV}, which is given by

$$\Xi_{NV} = \frac{(\boldsymbol{Z_f} + \boldsymbol{Z_i})\boldsymbol{A_{OL}}}{\boldsymbol{Z_i}(1 + \boldsymbol{A_{OL}}) + \boldsymbol{Z_f}}. \tag{38}$$

Figure 7(b) illustrates the variations in the most significant noise sources and total noise with frequency for the current-amplified 2 × 2 mm LTO device discussed above. The inset in this figure is a magnified section of the graph from 10 to 100 Hz, which illustrates that in this example, the amplifier current and feedback resistor Johnson noises are closely similar. A higher value of R_f would have produced a significantly lower feedback resistor Johnson noise. In this design, the device total noise is dominated by these two noise sources up to just below 100 Hz, above which the voltage noise takes over as being dominant. From a material selection point-of-view, the *tanδ* noise is not significant in this example. This illustrates the importance of the details of the device design, and especially passive component selection, in determining the total noise of the device.

The device detectivity D^* can be derived by combining the responsivity and the total noise. This is plotted as a function of frequency in Fig. 7(c), again compared with the JFET-amplified device. Note that although the responsivities vs frequency for the two devices peak at different frequencies and differ by more than an order-of-magnitude, the detectivities are similar in both magnitude and frequency responses. In this case, the JFET-amplified device is slightly better, with both devices showing a relatively flat response from 1 to 100 Hz, which is the range of greatest interest for most applications. Note that a different selection of R_f (say, 100 GΩ) would improve D^* for the current-amplified device so that both devices would have closely similar detectivities. This illustrates that choosing whether to use a voltage or current amplifier is more likely to be driven by consideration of the following electronics and determined by the system requirements and overall cost as much as signal-to-noise performance.

III. PYROELECTRIC MATERIALS AND THEIR FIGURES-OF-MERIT

Table SI in the supplementary material lists the basic characteristics of some commercial PIRDs using LTO as the pyroelectric material. (Note that the characteristics of the example device listed in Fig. 3(c) are similar to InfraTec 316.) All the PIRD elements are in the range of 0.5–3 mm in linear dimensions and are typically a few square mm in area. Most of the devices listed use a JFET as a voltage amplifier, but some employ OpAmp current amplifiers, which have much higher voltage responsivities than the voltage amplified devices but similar detectivities, as discussed above. All the devices are quite similar in element size and performance, and they mostly use the same pyroelectric material—LTO. The devices made by Pyreos use a sputtered thin film PZT-based thin film material. The ceramic-based devices made by Nippon Ceramic have been discontinued but are included here for completeness. As these are all from successful companies, it means that the device designs and performances satisfy the needs of the market. Nevertheless, research into new pyroelectric materials is a very active topic. A recent review of pyroelectric materials by Zhang *et al.*[52] indicated an average of over 250 papers published per year since 2000, covering all applications including IR sensing, energy recovery, and catalysis. About 60% of these were journal articles. A search on the terms "pyroelectric* and material*" on Web of Science for this article indicated about 68 papers published in 2000, rising to nearly 160 in 2021. Restricting this search to topics covering IR sensing applications still produced an average of about 20 papers per year from 2000 to the present date, or over 500 journal papers. Given that this is a substantial amount of research, it is fair to ask why most commercial PIRDs today use LTO as the active material when there are thousands of pyroelectrics available.

The PIRD engineer needs a way to conveniently decide which pyroelectric to choose to produce the best performance in a particular application. This problem has traditionally been addressed by using the device equations discussed above and the relevant materials' properties to derive "figures-of-merit" (FoM) that are supposed to be able to rank the possible materials according to their physical properties. The question was first addressed (as long ago as 1966) by Burdick and Arnold,[53] who derived a FoM for the signal-to-noise ratio (F_D), based on the assumption that the *tanδ* Johnson noise [Eq. (24)] was dominant,

$$F_D = \frac{p}{c'\sqrt{\varepsilon_o \varepsilon \tan\delta}}. \tag{39}$$

They used this to compare the likely relative performances of $BaTiO_3$ and triglycine sulfate (TGS). They pointed out the difficulties of reliably measuring *tanδ* at the lower end of the modulation frequencies used for their device measurements (15 Hz, 90 Hz, and 1 kHz). Liu[54] later referred to two further FoMs, which were directly linked to F_D, the appropriateness of each one depending on the capacitance of the element C_p relative to that of the input capacitance of the amplifier, C_a. For small values of C_p, the performance was predicted to be proportional to F_i,

$$F_i = \frac{p}{c'}. \tag{40}$$

For large values of C_p, the performance was predicted to be proportional to F_V,

$$F_i = \frac{p}{c'\varepsilon_o \varepsilon}. \tag{41}$$

© Author(s) 2023

However, it was considered that it would usually be possible to optimize the value of C_p by a good device design so that for most considerations, F_D would be the best FoM and, therefore, that it was important to minimize tanδ by the choice of the most-appropriate materials, by material design (e.g., through compositional doping) or by improvements to material processing.

Table I lists the relevant properties of a selection of some bulk ferroelectrics that have been used, or considered for use, in PIRDs, together with their basic properties at room temperature. Most of the parameters listed in this table already have been defined in this text. The only one that has not is the depolarization temperature (T_d). This is the temperature at which the material loses its ferroelectric polarization. Normally, this would be taken as being the same as the ferroelectric-to-paraelectric transition temperature or Curie temperature (T_C). However, some materials undergo depolarizing phase transitions below T_C, which leads to a value of $T_d < T_C$. These materials are discussed further below. Note that the maximum temperature at which a material can be operated or stored without significant loss of polarization can be significantly below T_d, and such temperatures should include processing temperatures, such as flow-soldering in system assembly.

A relatively small selection of materials out of the hundreds available has been chosen for consideration in this study. They are (referring to the materials by their codes for textual brevity) as follows.

LTO: this is a single crystal ferroelectric that is widely used in a range of applications in addition to PIRDs, including piezoelectric filters (surface and bulk waves)[84] and electro-optic devices.[85] Its ready availability, ease of processing, and moderate cost, combined with its high T_C, excellent stability, and good performance, make this the benchmark material for PIRD applications.

DTGS: deuterated triglycine sulfate is another single crystal material with a very long history of application in PIRDs. It is a water-soluble material, which makes for relatively easy growth, with a relatively high pyroelectric coefficient. It was the preferred target material for the pyroelectric vidicon,[86,87] which was at the heart of an early form of an uncooled thermal imager that was widely used in firefighting in the 1970s and 1980s. It has a relatively high pyroelectric coefficient and quite low dielectric constant and has been widely used in applications such as FTIR instrumentation. However, the water solubility requires specialist processing and the relatively low T_C means that it needs care in use. Many isomorphs have been grown (e.g., triglycine fluoberyllate[88]), and various dopants such as L-alanine[89] have been included in the crystals to make them less-susceptible to depoling during thermal excursions that may approach or exceed T_C. This thermal resilience is engendered by the formation of an internal bias field caused by the dopant ion. DTGS is included on this table as a representative of the family as the room-temperature properties are typical. Some devices using DLTGS-based materials are available commercially (see Table SI in the supplementary material).

P(70VDF-30TrFE) copolymer: this is a ferroelectric[90] copolymer between vinylidenefluoride and trifluoroethylene. T_C varies from 135 °C for 20%TrFE to 49 °C for 50%TrFE.[64] It is characterized by having a low p and a low ε, with is major advantages being the facts that it is chemically inert and easily cast from organic solvents to form thin films on a wide variety of substrates.

PZT25/75: this is an example of an oxide thin film directly deposited on silicon. It has been extensively researched for PIRDs[91,92] and used in commercial devices.[93] Pyroelectric thin film materials and their use in PIRDs will be considered in another critical review.

PCT:Mn: this is a ferroelectric ceramic based upon lead titanate that has been widely used for the manufacture of low cost PIRDs. It is discussed in greater detail in the next section.

PZFNTU: this is a ferroelectric ceramic based upon lead zirconate that has been used for the manufacture of a range of single element and array-based detectors.[22,94] It has the advantage of an electrical resistivity that can be readily varied through compositional doping. It is discussed in greater detail in the next section.

PMNT-based: these are a class of single crystals based on solid solutions between lead magnesium niobate and lead titanate that have been extensively studied for piezoelectric applications.[95] They are characterized by having high pyroelectric coefficients together with high dielectric constants and low losses. They are extensively discussed below.

NBT-based: these are materials (ceramics and single crystals) based on sodium bismuth titanate that are examples of materials being researched as lead-free pyroelectric materials. The pyroelectric properties are interesting, but reported values of T_C are quite low. They are discussed further below.

Evaluations of the three FoM F_i, F_V, and F_D have dominated discussions of the relative merits of different pyroelectric materials for PIRD applications for some decades, so it is worth undertaking a review of their practical relevance. All the authors who first derived the pyroelectric materials' FoM agree that they can only be expected to work well in quite specific circumstances. For example, F_V is derived from the expression for $\mathcal{R}_V$ of a voltage amplified device [Eq. (17)] and only applies at frequencies that are well above f_T and f_E and for devices where $C_p \gg C_A$.[13] F_i is generally taken to be most applicable for small area voltage amplified devices where $C_p \ll C_A$ or for devices using current amplifiers. The assumptions used in deriving F_D mean that it is only applicable at higher frequencies and where the dominant noise source comes from $tan\delta_p$.[13] Neumann *et al.*[96] have pointed out that, at low frequencies, the device noise is dominated by the input resistor Johnson noise N_{Rgi} [see Eq. (22) and Fig. 5] and that F_i is the best FoM to use in this region, while at high frequencies the amplifier voltage noise can dominate, so that here F_V would be most relevant. At intermediate frequencies, where the $tan\delta$ noise might dominate, then the best FoM to use would be F_D, although this would not be true once the $tan\delta$ noise drops below a certain level, which is determined by the levels of the other noise sources. At this point, $tan\delta$ becomes less relevant to device performance and it is pointless to waste effort on driving it lower. Even worse, over-stressing the importance of F_D as a FoM might lead to the selection of a material that is worse in other ways, such as thermal stability. Xu *et al.*[76] compared the properties of LTO with a $0.73Pb(Mg_{1/3}Nb_{2/3})O_3$-$0.27PbTiO_3$ (73PMNT/27PT) single crystal material and showed that for devices using 2.5 mm square, 20 μm thick elements in the 10–100 Hz frequency range, the noise for the LTO device is dominated by N_{Rgi}, while the noise for 73PMNT/27PT is dominated by the $tan\delta$ noise. The inspection of Fig. 5 shows that for a JFET-amplified device with the particular device

© Author(s) 2023

TABLE II. Crossover frequencies (in Hz) between input resistor noise (N_{Rgi}) vs $tan\delta$ noise (N_{Ji}) and the amplifier current noise (N_{iai}) vs $tan\delta$ noise (N_{Ji}) calculated for a JFET voltage-amplified device from the properties of some pyroelectric materials selected from Table I (frequencies are f_{RgJi} and f_{iaiJi}, respectively). (The calculations assume that R_g = 50 GW and N_{Ji} = 0.25 fAHz$^{-½}$.)

		Material		
Element linear dimensions (mm)	Crossover frequency for $tan\delta$ noise vs:	LTO	PZFN20T02U005	PIMNT: Mn (23/47/30) (111)
2 × 2	Gate resistor (f_{RgJi})	125 Hz	2 Hz	16 Hz
	Current (f_{iaiJi})	24 Hz	0.4 Hz	3 Hz
0.2 × 0.2	Gate resistor (f_{RgJi})	12.5 kHz	186 Hz	61 Hz
	Current (f_{iaiJi})	2.4 kHz	35 Hz	12 Hz

dimensions chosen, the $tan\delta$ noise for a LTO device only starts to dominate over N_{Rgi} at frequencies above about 125 Hz. This frequency is easy to calculate by placing $N_{Rgi} = N_{Ji}$ from Eqs. (22) and (24), and then the crossover frequency f_{RgJi} is given by

$$f_{RgJi} = \frac{d}{2\pi A R_g \varepsilon \varepsilon_o \tan\delta}. \tag{42}$$

Similarly, a crossover frequency f_{iaiJi} between $tan\delta$ noise and the amplifier current noise N_{iai} from Eq. (21) can be shown to be

$$f_{iaiJi} = \frac{N_{iai}^2 d}{8k\Theta\pi A \varepsilon \varepsilon_o \tan\delta}. \tag{43}$$

Table II tabulates these frequencies for three of the materials selected from Table I. There is a large range of crossover frequencies (from 0.4 Hz to >12 kHz), depending on the material used, the linear dimensions of the pyroelectric element, and whether the other dominant noise source comes from the Johnson noise of the gate input resistor or the current noise of the amplifier. Some of these frequencies fall within the range over which PIRDs are most-commonly used (0.1–100 Hz), but some are well-outside. This illustrates how difficult it can be to generalize which noise source will dominate the signal-to-noise performance and, hence, which of the FoM listed above might be the best one to use. Also note that the dielectric properties used in this illustration were typically measured at around 1 kHz, which is clearly inappropriate when the crossover frequencies concerned are mostly well below this. This illustrates another important point. There are many papers in which dielectric properties are measured at around 1 kHz, from which the authors calculate the pyroelectric FoMs and then go on to generalize about the likely usefulness of the materials concerned, often in comparison with other materials reported in the literature. Frequently, this is done without considering the appropriateness of the measurement frequency for the dielectric properties relative to the likely frequency of device use or which of the FoM are likely to be most representative of signal-to-noise performance, given the other noise sources in a device. This is a very important consideration for ferroelectrics, for which the dielectric properties can be strongly dependent on frequency, especially in the range of 0.1 Hz–1 kHz. Unfortunately, there are little dielectric property data available for many pyroelectric materials in the frequency range below 100 Hz. Nevertheless, we can use what data there are to explore how predicted device performances would change when it is used, rather than simply relying upon 1 kHz dielectric data and assuming that this is valid right across the frequency range of greatest interest for PIRDs.

Following Jonscher,[97] we can write the AC conductivity $\sigma(\omega)$ as

$$\sigma(\omega) = \sigma_o + \omega\varepsilon_o\varepsilon''(\omega), \tag{44}$$

where $\varepsilon''(\omega)$ is the imaginary part of the relative permittivity and σ_o is the conductivity close to DC. We can also express $tan\delta_i$ as a function of frequency as

$$tan\delta_i(f) = \frac{\sigma(\omega)}{\omega\varepsilon_o\varepsilon'(\omega)} = \frac{\sigma(f)}{2\pi f\varepsilon_o\varepsilon'(f)} = \frac{2\pi f\varepsilon_o\varepsilon''(f) + \sigma_o}{2\pi f\varepsilon_o\varepsilon'(f)}, \tag{45}$$

where $\varepsilon'(f)$ is the real part of the relative permittivity.

One of the materials listed in Table I, a ceramic material[98] with the following composition: $Pb[Zr_{1-x-y}(Fe_{½}Nb_{½})_xTi_y]_{1-z}U_zO_3$; x = 0.2, y = 0.02, z = 0.005, coded PZFNTU, has been used extensively in single element PIRDs[72] and PIRD arrays.[99] It was engineered to have very good pyroelectric properties as well as a DC resistivity that was well-controlled in the range of 4–8 × 10^9 Ω m. This permitted the input resistor at the FET gate (R_G) to be eliminated as a discrete component. The ability to eliminate R_G is particularly important when making 1D and 2D arrays, and the material has seen use in 2D arrays for use in, e.g., thermal imagers for firefighting[100] and commercial footfall sensors.[22] The devices illustrated in the images shown in Fig. 2 were made using this material. The dielectric properties of this material were well characterized at low frequencies[43] (Fig. 8). The AC conductivity ($\sigma(f)$) experimental data [Fig. 8(a)] are modeled using

$$\sigma(f) = \sigma_o\left[1 + \left(\frac{f}{f_o}\right)^{\alpha}\right]^{\beta}, \tag{46}$$

where f_o is a turn-over frequency and α and β are exponents. The model fits the data very well with the parameters presented in the figure. Note that according to Jonscher,[97] we would expect $\sigma(f) \propto f^m$ with $m = \alpha\beta < 1$. In the case of the parameters used to fit the PZFNTU data plotted in Fig. 8(a), $m = 0.63$, as expected for a system dominated by the hopping conduction of charge carriers.[43] The real part of the relative permittivity ($\varepsilon'(f)$) is plotted in Fig. 9(b). This can be modeled with

$$\varepsilon'(f) = \varepsilon'_K\left[1 + \left(\frac{f_e}{f}\right)^{a}\right]^{b}, \tag{47}$$

where f_e is a turn-over frequency and a and b are exponents. Again,

© Author(s) 2023

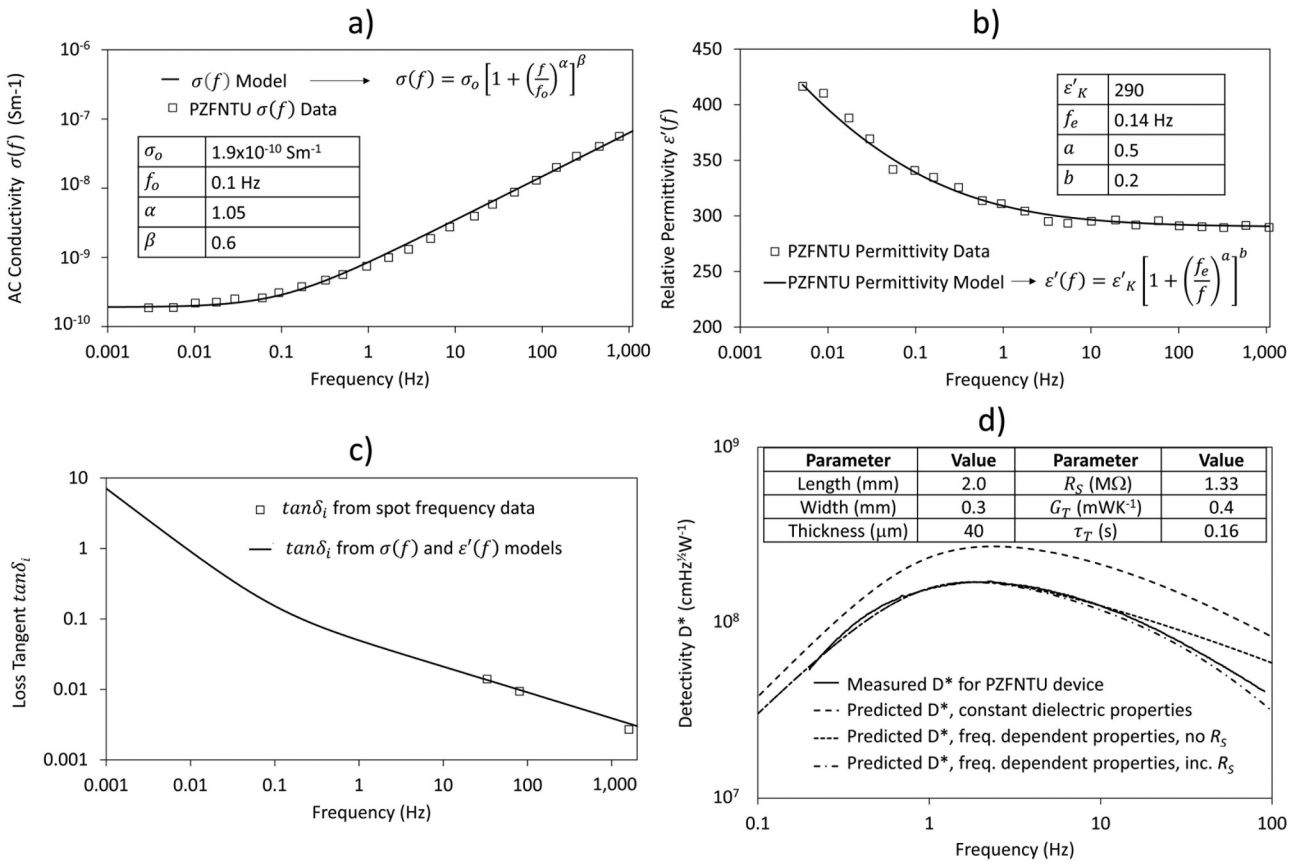

FIG. 8. Dielectric properties of PZFNTU pyroelectric ceramics as functions of frequency: (a) AC conductivity $\sigma(f)$ with experimental data[43] (open squares) and model (solid line) fitted according to Eq. (45)—shown in the figure—and parameter values given; (b) real part of the dielectric relative permittivity with experimental data[43] (open squares) and model (solid line) fitted according to Eq. (46)—shown in the figure—and parameter values given; [experimental data in (a) and (b) reproduced with permission from Whatmore, Ferroelectrics **49**, 201–210 (1983). Copyright 1993 Taylor and Francis Ltd, http://www.tandfonline.com]. (c) The intrinsic dielectric loss tangent $tan\delta_i(f)$ calculated from the models shown in (a) and (b), together with spot-frequency experimental data;[14,72] (d) comparison of the measured D^* for a 2 × 0.3 mm area, 40 μm thick PZFNTU device taken from Putley[33] (device 52) with predictions based on different data sets of the dielectric properties (see text). Experimental data in (d) is reproduced with permission from Putley, Infrared Phys. **20**, 139–147 (1980). Copyright 1980 Elsevier.

the model fits the data very well with the parameters presented in the figure.

We can use the $\sigma(f)$ and $\varepsilon'(f)$ models to calculate a continuous function for $tan\delta_i(f)$ according to Eq. (45). This is plotted in Fig. 8(c), together with spot-frequency values of $tan\delta_i(f)$ measured separately using capacitance bridges.[14,72] There is excellent agreement between the model-based calculations and the experimental data. We can, therefore, use the $\sigma(f)$ and $\varepsilon'(f)$ models with confidence to give $tan\delta_i(f)$ values for PIRD performance predictions.

Putley[33] published the performance figures for a 2×0.3 mm by 40 μm thick device using PZFNTU and a BF800 JFET amplifier with an equivalent input current noise of 0.3 fA $Hz^{-½}$. (The voltage noise for this amplifier is not significant in the frequency range reported.) The results for D^* are shown in Fig. 8(d), together with the model predictions using: first, the dielectric properties measured at 1592 Hz for this material (see Table I) but assumed to be constant across the whole frequency range, second the dielectric properties measured as functions of frequency and shown in Figs. 8(a) and 8(c) but assuming zero R_S, and third, these frequency-dependent dielectric properties but with $R_S = 1.33$ MΩ. The other material parameters were all as listed for this material in Table I and the electrode emissivity was set so $\eta = 0.45$. The values of the other relevant device parameters (e.g., G_T and τ_T) are indicated in the figure and are in reasonable agreement with the values calculated by Putley[33] for this device. It is clear that the use of the high-frequency, frequency-independent dielectric properties gives relatively poor agreement with the reported experimental data. The frequency-dependent dielectric data give good agreement with the experimental data, up to just over 10 Hz, at which point the predictions start to diverge from the data. The inclusion of the indicated value of R_S [and, therefore, a non-zero value of $tan\delta_{RS}$—see

© Author(s) 2023

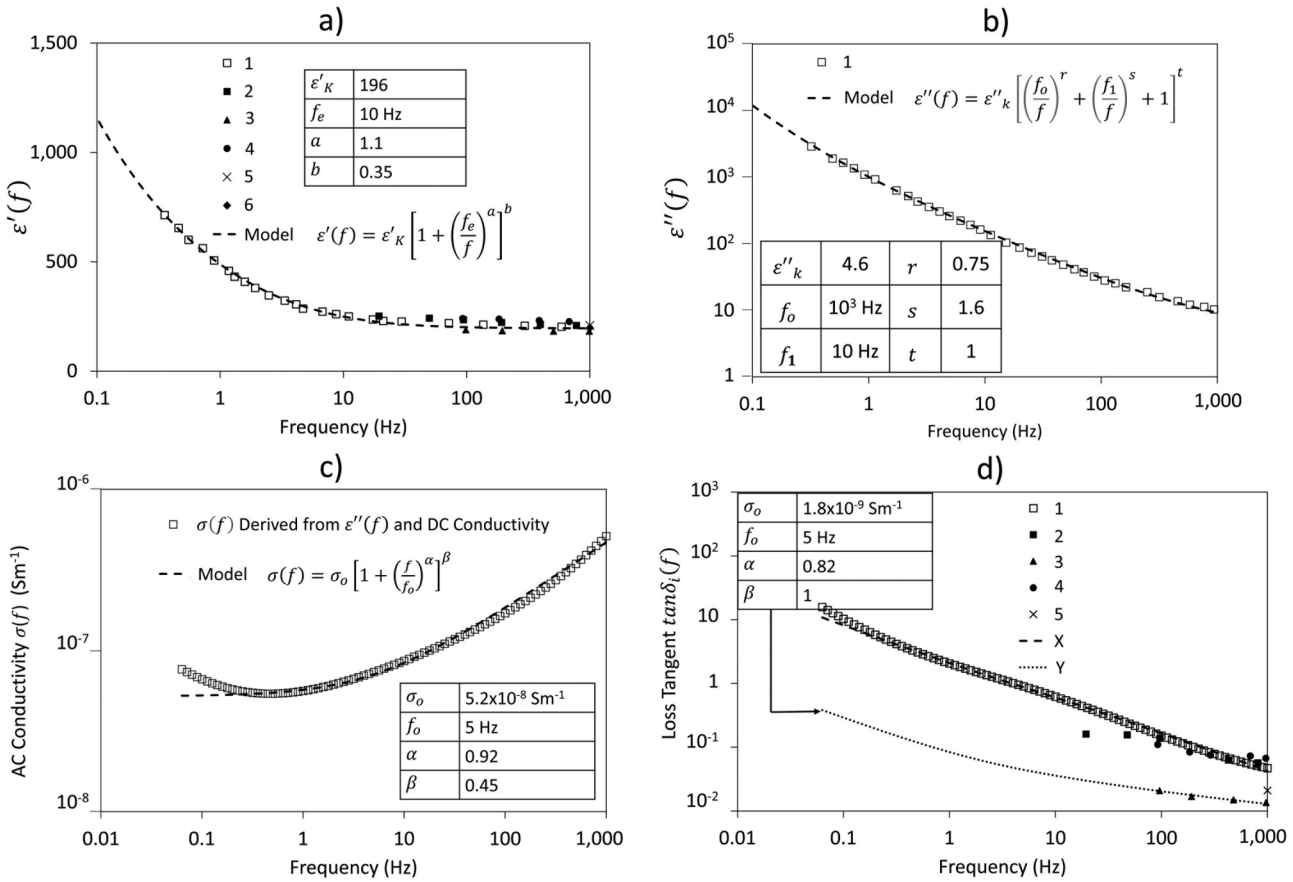

FIG. 9. Dielectric properties of PCT $(Pb_{(1-x)}Ca_x[(Co_{½}W_{½})_yTi_{1-y}]O_3$; x = 0.24–0.27, y = 0.04 ceramics as functions of frequency. The ceramics are doped with a variety of elements as indicated below. (a) Real part of the dielectric relative permittivity, $\varepsilon'(f)$; (b) imaginary part of the dielectric relative permittivity, $\varepsilon''(f)$; (c) AC conductivity $\sigma(f)$ derived from $\varepsilon''(f)$ and the DC conductivity reported by Jiménez *et al.*[102]; (d) intrinsic loss tangents $tan\delta_i(f)$ from the different sources compared with two models. Line X shows the $tan\delta_i(f)$ function calculated from the $\varepsilon'(f)$ model in Fig. 9(a) and $\sigma(f)$ in Fig. 9(c). Line Y shows the $tan\delta_i(f)$ function calculated from the $\varepsilon'(f)$ model in Fig. 9(a) and $\sigma(f)$ calculated using the model parameters shown in the figure. The graphs include data from a variety of literature sources, which are numbered as follows: 1: PCT y = 0.24 doped with 1% Mn: data reproduced with permission from Journal of Physics and Chemistry of Solids, **57**, 389 (1996); Copyright 1996 Elsevier; 2: Undoped PCT y = 0.27, 3: PCT y = 0.27 doped with 1 Mol. % MnO_2, 4: PCT y = 0.27 doped with 1 Mol. % Ni; data in 2, 3, and 4 reproduced with permission from Ferroelectrics, **118**, 111 (1991),[68] Copyright 1991 Taylor and Francis Ltd, http://www.tandfonline.com., 5: PCT y = 0.24 doped with 0.3 Wt. % (1.1 Mol. %) MnO and 0.4 Wt. % (1.5 Mol. %) NiO from Yamashita *et al.*[101] 6: PCT y = 0.24 doped with Mn and Ni from Ichinose *et al.*[70]

Eq. (27)] gives excellent agreement across the whole frequency range. In the original report, Putley[33] had to include a frequency-constant value of $tan\delta = 0.016$ to get agreement between the performance predictions and experiments. This is much higher than the value measured at 1592 Hz, but no explanation was given for this adjustment. The inclusion of an electrode surface resistance R_S gives a reasonable explanation for the higher-than-expected high frequency value of $tan\delta$, but the R_S value needed is high and may indicate relatively poor electrode manufacture in this case. The conclusion from this work is that the dielectric properties of ferroelectric materials can be strongly frequency dependent across the range of greatest interest for PIRD operation and, therefore, that this dependence should be measured if good agreement is to be expected between predictions of performance and experimentally measured values. However, reports of such measurements are rare. Only occasionally are point-frequency measurements of dielectric properties seen at sub-100 Hz frequencies, and complete dielectric spectroscopy data of the type shown in Figs. 8(a) and 8(b) are even more unusual.

Modified lead titanate ceramic $Pb_{(1-x)}Ca_x[(Co_{½}W_{½})_yTi_{1-y}]O_3$; x = 0.24 to 0.27, y = 0.04 (PCT), doped with various transition metal ions, is another example of a ferroelectric ceramic for which some broad-frequency spectrum dielectric data are available. It has been studied by several authors for piezoelectric and PIRD applications. Figure 9 plots and compares several sets of dielectric data taken from the literature. Yamashita *et al.*[101] were some of the first authors to study the piezoelectric and dielectric properties of PCT with x = 0.24 and doped 0.3 wt. % MnO and 0.4 wt. % NiO

© Author(s) 2023

(corresponding to 1.1 at. % Mn and 1.5 at. %Ni, respectively), while Ichinose *et al.*[70] were the first to publish the details of PIRDs made using this ceramic. The broadest frequency data for PCT with x = 0.24 and doped with 1% Mn comes from Jiménez *et al.*,[102] who measured the dielectric properties down to 0.01 Hz and give a value of $8 \times 10^9\ \Omega$ m for DC resistivity (ρ_o) implying a DC conductivity $\sigma_o = 1.25 \times 10^{-10}\ \mathrm{Sm}^{-1}$. (The paper does not indicate whether the ceramic is doped with 1 wt. % Mn or 1 at. % Mn.) Nadoliisky *et al.*[68] measured the dielectric properties of PCT with x = 0.27, both undoped and doped with 1 mol. % MnO_2 or 1 mol. % NiO at frequencies down to about 20 Hz. Figure 9(a) plots the real part of the relative dielectric permittivity $\varepsilon'(f)$ as a function of frequency from all these sources. It can be seen that there is excellent agreement between them and that the model for $\varepsilon'(f)$ given in Eq. (46) fits the data very well, with the relevant constants quoted in the figure. Figure 9(b) plots the imaginary part of the relative dielectric permittivity $\varepsilon''(f)$ as a function of frequency from Jiménez *et al.*[102] This has been fitted very well to a model,

$$\varepsilon''(f) = \varepsilon''_k\left[\left(\frac{f_o}{f}\right)^r + \left(\frac{f_1}{f}\right)^s + 1\right]^t, \tag{48}$$

with the relevant constants given in the figure. Equation (44) can then be used to derive $\sigma(f)$ from $\varepsilon''(f)$ and σ_o, which is plotted in Fig. 9(c) and fitted to the model in Eq. (46). The relevant constants are again quoted in the figure. Finally, $\tan\delta_i(f)$ can be derived from the $\sigma(f)$ and $\varepsilon''(f)$ functions obtained from the models fitted to the data from Jiménez *et al.* using Eq. (45). This is plotted in Fig. 9(d). Values of $\tan\delta_i(f)$ from the other sources mentioned above are also plotted in this figure. It can be seen that there is good agreement and overlap between the sets of data from these disparate sources, but it is interesting to note that the Mn doped sample reported by Nadoliisky *et al.*[68] and the Mn/Ni doped sample reported by Yamashita *et al.*[101] have significantly lower losses than the Mn-doped and Ni-doped samples reported by Jiménez *et al.*[102] The reasons for this are unclear but could point to differences in sample preparation, and it is a pity that wider-frequency dielectric data for the lower-loss samples are unavailable. Nevertheless, the data available indicate that we can use models of the type derived from the broad-spectrum data from Jiménez *et al.*[102] for the predictions of the likely performances of other PCT-type ceramics in PIRDs and in Fig. 9(d), we show $tan\delta_i(f)$ modeled with a modified $\sigma(f)$ function designed to fit the lower loss measured by Nadoliisky *et al.*[68] The constants for this model are reported in the figure.

Single crystals based on the lead magnesium niobate–lead titanate solid solution system [$xPbMg_{1/3}Nb_{2/3}O_3$-$(1-x)PbTiO_3$—coded PMNTx/(1−x) in Table I] form a further class of new materials that has excited considerable interest for applications in PIRDs. Following-on from studies showing exceptional piezoelectric properties in single crystals of lead zinc niobate–lead titanate (PZNT),[103] PMNT crystals were also shown to be excellent piezoelectrics by Shrout *et al.*[95] and their growth and properties have been studied extensively.[104] Davis *et al.*[105] were the first to show that PZNT and PMNT crystals possessed very high pyroelectric coefficients ($500\ \mu\mathrm{C\,m^{-2}\,K^{-1}}$ or more). Since then, many authors have studied the pyroelectric properties and potential PIRD applications of crystals of PMNT[75–78] and $xPb(In_{1/2}Nb_{1/2})O_3$-$yPbMg_{1/3}Nb_{2/3}O_3$-$(1-x-y)PbTiO_3$ [coded PIMNTx/y/(1−x−y) in Table I].[79,80,96,106,107] The properties of some of these materials are listed in Table I. Mn-doping has been explored for dielectric loss reduction in these materials (giving crystals coded: Mn in Table I), and the frequency dependences of the dielectric losses in these crystals have been reported,[80] together with the detectivities of voltage and current mode PIRDs made using them.[80,96] One issue with crystals of this type is that their compositions have usually been fixed to optimize their piezoelectric properties, placing them close to a rhombohedral-to-tetragonal phase boundary (generally called a morphotropic phase boundary, or MPB) in the compositional phase diagram. The crystals are often in the rhombohedral phase at room temperature and pass through a phase transition to a tetragonal phase on heating. They depolarize at this temperature (T_d), which is a serious issue in device manufacture and use, as will be discussed below.

Figures 10(a) and 10(b) plot the modeled for D^* for devices made with (111) oriented, 30 μm thick slices of PIMNT:Mn23/47/30 crystals for both voltage and current-amplified devices using both constant (1 kHz) and full-frequency (FF) dielectric data using the published materials' properties. The results agree well with the published D^* data.[80] The models have also been used to compare the relative contributions of the *tanδ* noise with the amplifier voltage noise sources in the case of the JFET-amplified device, which are shown in Fig. 10(c). The model assumes that the size of the detector element was 2×2.2 mm, the material had the basic properties as listed in Table I, the JFET had similar characteristics to the standard InfraTec JFET device and that the current amplifier had similar characteristics to the standard InfraTec OpAmp,[47] with an equivalent input current noise of $0.6\ \mathrm{fA\,Hz^{-1/2}}$. The input-referred voltage noise of the amplifier, $\overline{e_n}(f)$ was modeled with the function $\overline{e_n}(f) = \overline{e_n}\left(1 + \left(\frac{f_o}{f}\right)\right)$ with $\overline{e_n} = 12\ \mathrm{nVHz^{1/2}}$ and $f_o = 20$ Hz. Note that this value of $\overline{e_n}$, which is required to give good agreement between the modeled and observed data above 50 Hz, is slightly lower than the datasheet value of $19\ \mathrm{nV\,Hz^{1/2}}$. This is not significant in the current discussion. The model for $tan\delta_i(f)$ was achieved by modeling the AC conductivity $\sigma(f)$ using Eq. (46) with $\sigma_o = 1.5 \times 10^{-10}\ \mathrm{Sm^{-1}}$, $f_o = 14$ Hz, $\alpha = 0.75$, and $\beta = 1.25$. In both cases, $R_f = R_g = 50\ \mathrm{G\Omega}$, $R_S = 300\ \Omega$, (which is insignificant), and $\tau_T = 232$ ms, with $\eta = 0.7$ for the JFET-amplified device and 0.8 for the current-amplified device. In the case of the voltage-amplified device, there is a small but significant difference between the 1 kHz and FF model predictions for D^* below 20 Hz, with the FF loss giving better agreement with the experimental data. The reason for this is clear from Fig. 10(c). Above 15 Hz, the total noise is dominated by the amplifier voltage noise. Below this frequency, the *tanδ* noise is the most significant noise source in the case of the FF dielectric data. In the case of the 1 kHz dielectric data, the *tanδ* noise is also dominant below 14 Hz but is significantly lower than the *tanδ* noise from the FF data. Clearly, in the voltage-amplified case, it is important to use the FF dielectric data to get a good prediction of device performance across all frequencies. On the other hand, for the current-amplified device, both 1 kHz and FF models for D^* gave very similar results [see

© Author(s) 2023

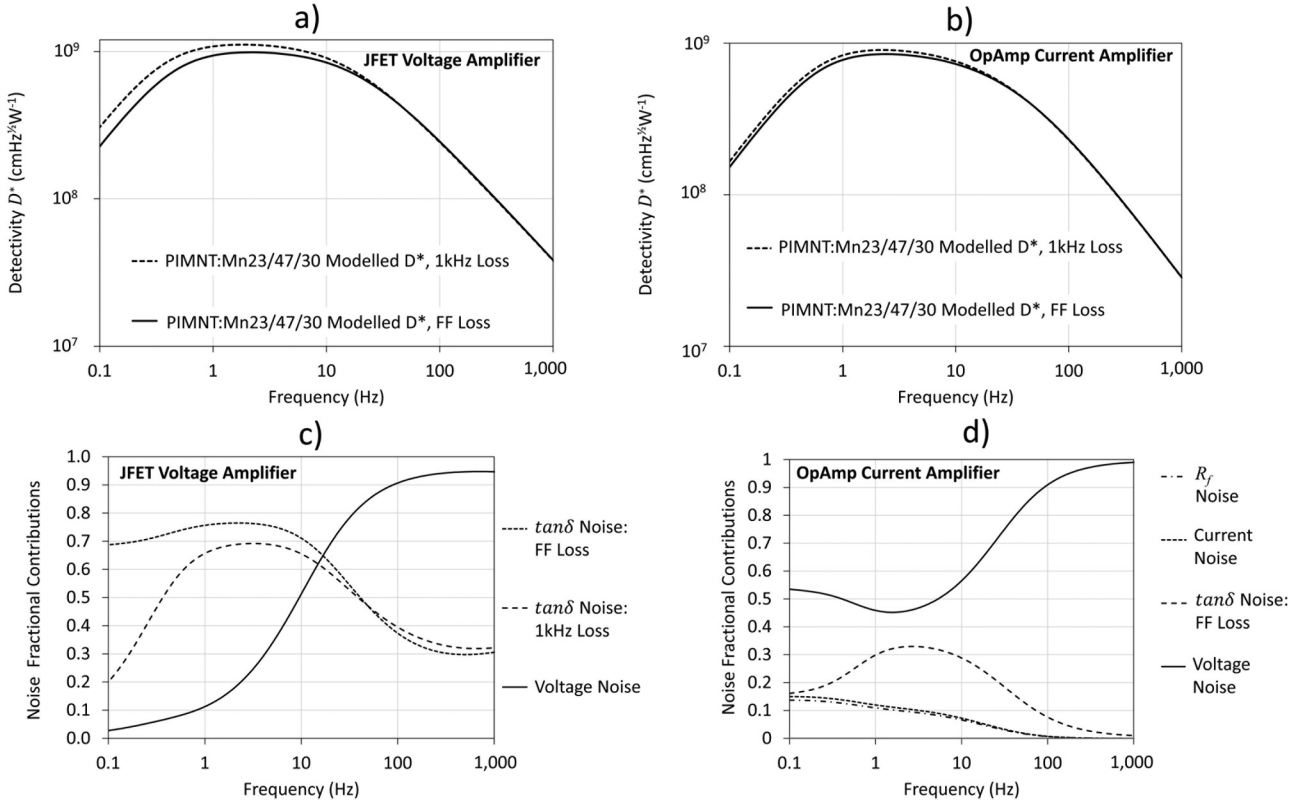

FIG. 10. Models (this work) for detectivities (D^*) of PIRDs made using PIMNT:Mn23/47/30 crystals for (a) JFET voltage and (b) current amplifiers. The models are calculated using both constant (1 kHz) and full-frequency (FF) dielectric loss data,[80] assuming a constant value for $\varepsilon'(f)$ of 570 (see Table I). (c) Comparison of the fractional contributions to total noise of the JFET-amplified device for the 1 kHz and FF dielectric loss data with the voltage noise. (d) Comparison of the fractional contributions to total noise of the most significant noise sources in the current-amplified device for the FF dielectric loss data.

Fig. 10(b)] and both agreed well with the published data. This is because the amplifier voltage noise dominates at all frequencies, although the $tan\delta$ noise also makes a significant contribution [see Fig. 10(d)]. The other devices using PMN-PT:Mn72/28 and PIMNT34/34/32 as reported by Yao *et al.*[80] were also modeled using both fixed (1 kHz) and FF dielectric data, yielding similar results. This example illustrates that it is vital to take account of all the noise sources when modeling D^*. Having a FF model of the dielectric properties can be very important if an accurate picture of the device performance is wanted, but it is also important to take account of all the other potential noise sources, as the $tan\delta$ noise may not be the most significant source, as is often assumed, even in the mid-frequency range.

In the case of LTO, there are range of values for the 1 kHz dielectric loss reported at ambient temperatures (see Table I), but there is very little data on the low frequency dependence of the dielectric properties at ambient temperatures. This may be a little surprising at first sight, given the technological importance of the material, but the accurate measurement of low losses at very low frequencies is difficult. Stokowski[39] measured $tan\delta$ for congruent-composition LTO down to 10 Hz, and it is possible to subtract the thermal loss and extract $tan\delta_i(f)$ from the data presented in this paper. Schossig *et al.*[31] measured the dielectric loss of this material as a function of wafer thickness down to 100 Hz. The results of their measurements are plotted in Fig. 11(a). The loss measured by Schossig *et al.*[31] is significantly higher than the intrinsic loss reported by Stokowski,[39] especially at low frequencies. The reasons for this difference are not clear but could be due to differences in sample preparation between the two sets of work. The report by Schossig *et al.* indicates a strong dependence of intrinsic loss as the thickness falls below 10 μm, an effect which was ascribed to damaged surface layers. Stokowski's work indicates a rising loss at low frequencies. This is easily explained. Consider the effects of there being a non-zero "DC" conductivity $\sigma_o = \rho_o^{-1}$. Even if the real (ε') and imaginary (ε'') parts of the relative permittivity are frequency independent, $\tan\delta_i$ will show a frequency dependence given by $tan\delta_i(f) = \frac{\varepsilon''}{\varepsilon'} + \frac{\sigma_o}{\omega\varepsilon_o\varepsilon'} = tan\delta_i(HF) + \frac{\sigma_o}{\omega\varepsilon_o\varepsilon'}$, where $tan\delta_i(HF)$ is the intrinsic loss tangent at high frequencies. Two values have been reported for ρ_o: $1.15 \times 10^{13}\,\Omega\,m$[55] and $5.35 \times 10^{12}\,\Omega\,m$.[108] Figure 11(b) plots the curves for $tan\delta_i(f)$ calculated by assuming these values of ρ_o, together with a curve for $\rho_o = 8 \times 10^{11}\,\Omega m$.

© Author(s) 2023

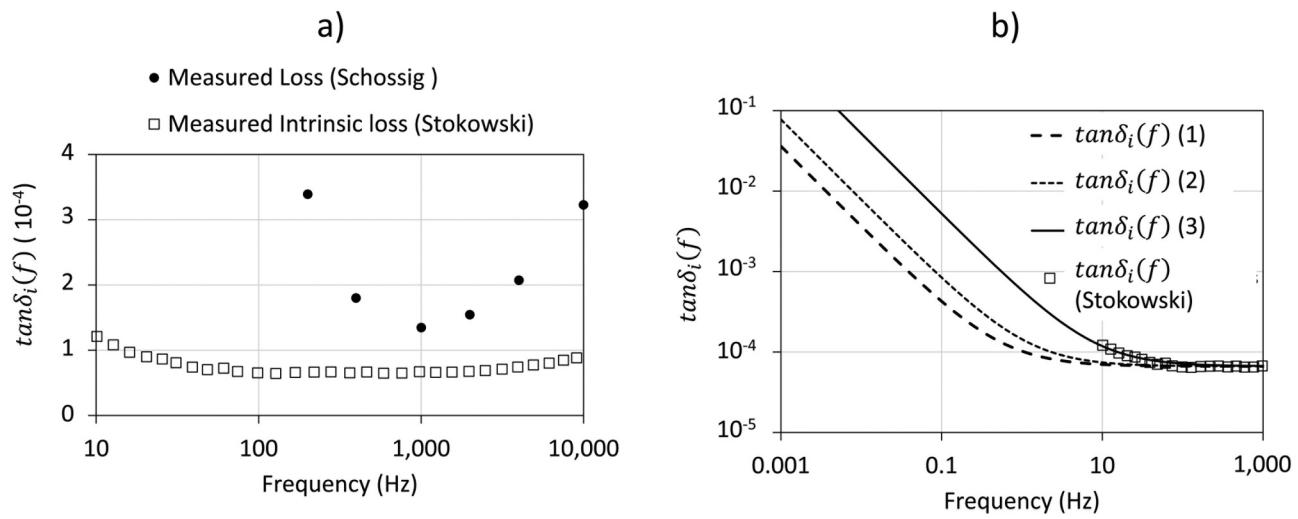

FIG. 11. Reported and modeled $tan\delta_i(f)$ data for $LiTaO_3$. a) $tan\delta_i(f)$ data derived from Stokowski[39] for 120 μm thick material and Schossig *et al.*[31] for a 20 μm thick material; (b) modeled $tan\delta_i(f)$ data using different values of DC resistivities taken from two literature sources and a value, which gives the best fit to the data: (1) $\rho_o = 1.15 \times 10^{13}$ Ωm[55]; (2) $\rho_o = 5.35 \times 10^{12}$ Ωm[108]; (3) $\rho_o = 8 \times 10^{11}$ Ωm when compared to the $tan\delta_i(f)$ data extracted from Stokowski.[39] Data reproduced with permission from Infrared Physics and Technology, **63**, 7 (2014). Copyright 2014 Elsevier.

This is a little lower than the literature values but gives a better fit to the intrinsic loss data derived from Stokowski.[39] All of these give an intrinsic loss that rises rapidly (as $1/f$) at sufficiently low frequencies when $\frac{\sigma_o}{\omega\epsilon_o\epsilon'} \gg \frac{\epsilon''}{\epsilon'}$. From Fig. 11(b), this appears to be between 0.1 and 10 Hz, a range that is of considerable interest for many real-world PIRD applications and, thus, it is important to take account of this effect when making device performance calculations. Neumann *et al.*[96] have compared the responsivities and detectivities for LTO and PIMNT:Mn23/47/30 (111) PIRDs using current amplifiers. These data have been extracted and compared with models of the performance parameters calculated using the equations above with the full-frequency dielectric data for the two materials discussed in this paper (see Table I). The comparisons are given in Figs. 12(a) and 12(b). The device parameters used are given in the figure caption. There is excellent agreement between data and models, giving good confidence in both the models used and the materials data and device parameters. The relative magnitudes of the principal noise sources are reported in each case in Fig. 12(c) for the LTO device and Fig. 12(d) for the PIMNT:Mn23/47/30 (111) device. It can be seen from these figures that the $tan\delta$ noise is insignificant for the LTO device, with the noise being dominated at low frequencies by the Johnson noise in the feedback resistor and at frequencies above about 180 Hz by the amplifier current noise. On the other hand, for the PIMNT:Mn23/47/30 (111) device, the $tan\delta$ noise dominates between about 1.4 and 20 Hz, a frequency range where many PIRDs are used.

This case illustrates an important issue when discussing the possible use of different pyroelectric materials in PIRDs. It is impossible to generalize and say that one material will be much better than another in a given application simply because it has a very low dielectric loss, which gives a high F_D [Eq. (39)]. In this case, the LTO has such a low $tan\delta$ that this source of noise ceases to be important in comparison with two other sources of noise that are unrelated to the properties of the pyroelectric material. It is worth, therefore, analyzing the usefulness of the pyroelectric FoMs in predicting the real-world performance of PIRDs. This analysis is the subject of the next section.

IV. PYROELECTRIC FoM UTILITY

The above discussion has established confidence in the ability of our device models to accurately predict the responsivities and noises for specific device configurations when used with the properties and FF dielectric data for the materials listed in Table I. Hence, they can be used to test the usefulness of the pyroelectric FoMs F_i, F_V, and F_D [described by Eqs. (40), (41), and (39), respectively] for the "ranking" of pyroelectric materials for use in PIRDs. When doing this, it must be borne in mind that PIRDs are commonly used in detection applications (e.g., for fires or intruders) where the system is designed to detect a signal that occurs within a given bandwidth rather than at a single frequency. (An exception to this would be an application such as IR spectroscopy where the radiation is modulated at a known frequency and the resulting output signal detected by an amplifier with narrow bandwidth.) Accordingly, a test has been designed so that the predicted detectivity is integrated over a given bandwidth bounded by frequencies f_1 and f_2, to give an "integrated detectivity" defined as

$$D_i^* = \sqrt{\frac{A}{\int_{f_1}^{f_2} (NEP)^2}}. \tag{49}$$

This has been done for both voltage and current amplifier configurations and for different sizes of the detector element. The

© Author(s) 2023

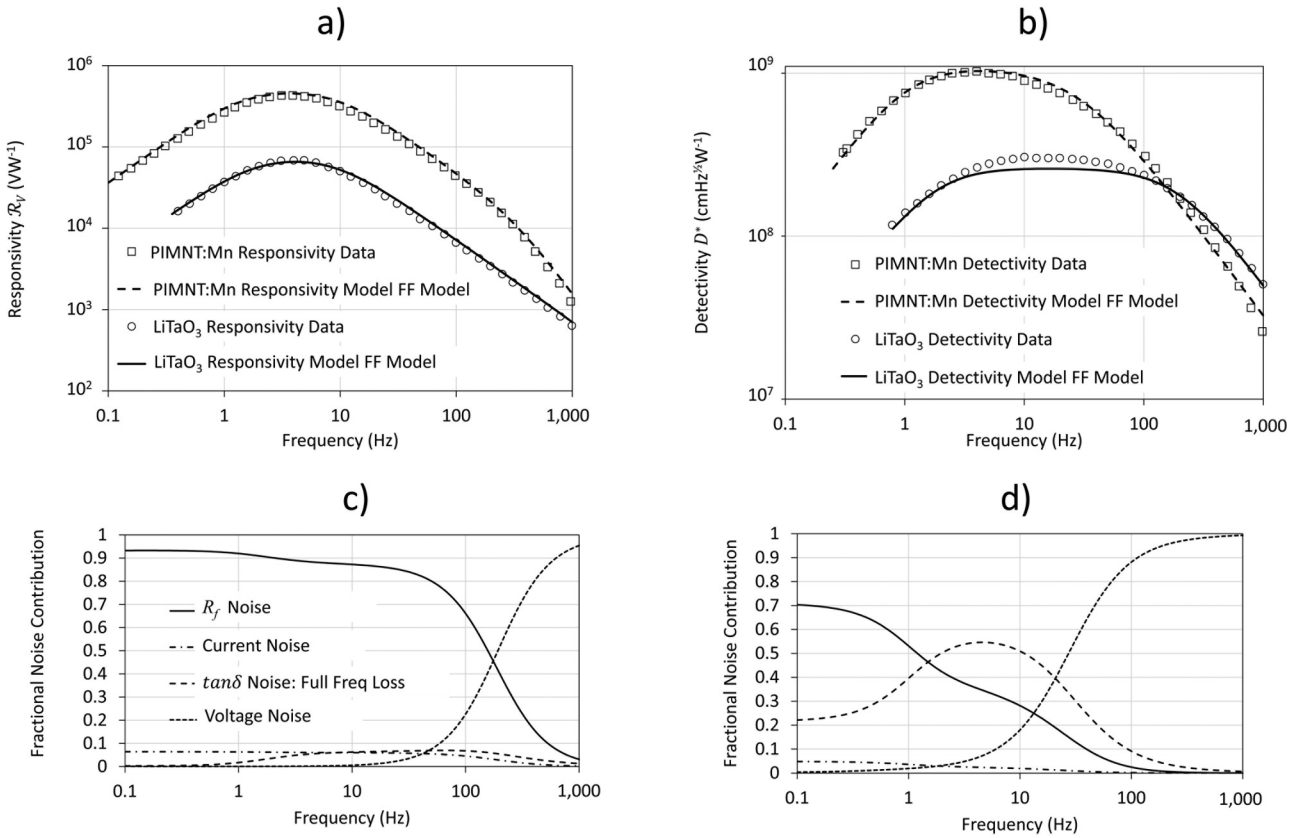

FIG. 12. A comparison of (a) responsivity, (b) detectivity, and (c,d) noise data for current amplified PIRDs using PIMNT:Mn23/47/30 (111) and $LiTaO_3$ (LTO) single crystal materials[96] compared with models derived using the full-frequency (FF) dielectric data presented in Table II. The experimental data in (a) and (b) were reproduced from APL Materials **9**, 021106 (2021) with the permission of AIP Publishing. (c) fractional contributions of the principal noise sources for the LTO device calculated and (d) same noise sources for the PIMNT:Mn device, both calculated with FF dielectric data. Note that the same legend is used for the different noise sources in (c) and (d). In both cases, the device parameters assumed in the models were as follows: dimensions: 1 × 1 mm area and 25 μm thickness; TI TLC2252 OpAmp with 50 GΩ and 0.35 pF feedback resistor and capacitor, respectively, surface resistivity 100 Ω/square, thermal conductance and η set at 90 μWK^{-1} and 70%, respectively, for the LTO device; 60 μWK^{-1} and 90% for the PIMNT:Mn device.

computed values of D_i^* for each bandwidth can be compared graphically with the values of F_i, F_V, and F_D for the different materials selected for test and a "goodness of fit" evaluated using R^2 from linear regression for each graph. This gives a good test of the linear correlation between the predicted performance parameter and a particular FoM. F_i is independent of frequency because it is only dependent on the pyroelectric coefficient and volume specific heat. However, F_V and F_D are frequency dependent. They are often computed using dielectric properties measured at a relatively high frequency (e.g., 1 kHz), because such measurements are simple and convenient. However, the dielectric properties are not then representative of the low frequencies at which PIRDs are most-commonly used, and therefore, the validity of the resulting FoMs may be called into question. Alternatively, F_V and F_D could be computed using dielectric properties measured at a lower frequency (e.g., 32 Hz). which would be much closer to the frequencies at which PIRDs are most-commonly used. However, such low frequency dielectric measurements are harder to accomplish reliably, especially for low loss materials. We can use this study to determine whether it is really necessary to make low frequency dielectric measurements when undertaking an evaluation of the FoMs. D_i^* would be most relevant in applications where the system noise is dominated by the intrinsic noise in the PIRD. The voltage responsivities $\mathcal{R}_V^a$ averaged over the same bandwidths can also be calculated and tested against the FoM values in a similar way. This would be most relevant in applications where the system noise is dominated by the noise in the electronics coming after the PIRD element.

Six materials were selected from Table I for the calculations. These were LTO, DTGS, P(70VDF-30TrFE), PZFN20T02U005, PCT24:Mn, and PIMNT:Mn (23/47/30) (111), which are all materials that have been used for practical PIRDs for which reliable dielectric property data are available over a sufficiently broad range of frequencies. They also give a wide range of FoM values so that the correlation can be properly tested. The parameters used for

© Author(s) 2023

modeling the dielectric properties over the full frequency ranges are given in Table III.

The bandwidths selected for the integration and averaging are

- 0.1 Hz–10 Hz, which covers many of the low-frequency motion-sensing applications and is a range to which F_i would normally be applied,
- 10 Hz–100 Hz, which covers the medium frequency range of some flame sensing applications and some "chopped" applications such as thermal imaging and is a range to which F_D would normally be applied,
- 100 Hz–1 kHz, which covers high frequency applications such as pulse detection and is a range to which F_V would normally be applied.

Two sizes of detector element have been chosen: 2×2 mm, which is in the middle of the range for the majority of commercial PIRDs (see Table SI) and 0.2×0.2 mm, which is the same order-of-magnitude as the element size in many pyroelectric arrays, e.g., those used in such applications as footfall sensing.[13,14] Element thickness was set at 30 μm, which is appropriate for a bulk material. For the voltage amplifier, the characteristics were taken from the datasheet of a PIRD manufacturer (InfraTec) as their standard device JFET,[47] with $R_g = 50$ GΩ. For the current amplifier, the characteristics were those of a low noise OpAmp similar to that of "OpAmp 2" described by InfraTec in their "Pyroelectric Library,"[47] which is similar to the Texas Instruments TLC2252, with $R_f = 50$ GΩ and $C = 0.35$ pF. The thermal conductance G_T of the 2×2 mm elements was set at 1.5 mW K^{-1}, while for the 0.2×0.2 mm elements, G_T was set at 0.5 mW K^{-1}. η has been set at 70% for all the devices.

Figure 13 shows a selection of four graphs of this type plotted for the materials chosen. Also plotted in each graph in this figure is a straight line fitted to the data using linear regression. The equation and the relevant R^2 value is also given for each line. It can be seen immediately that the quality of fit is extremely variable. It is clear from Fig. 13(a) that there is a general trend for D_i^* in a 2×2 mm voltage-amplified device at low frequencies to increase with F_i, as might be expected, although there is a lot of scatter in the points, so $R^2 < 75\%$, and the trend is far from completely convincing. Looking at Fig. 12(b), the linear relationship between D_i^* at high frequencies and F_D (1 kHz) is even less convincing as $R^2 < 58\%$. Looking at Figs. 13(c) and 13(d), which concern a 0.2×0.2 mm current-amplified device, we can see from Fig. 13(c) that there is an excellent linear fit between the average responsivity $\mathcal{R}_V^a$ at medium frequencies and F_i. This is an unsurprising result because F_i is proportional to the pyroelectric coefficient and, thus, gives a direct measure of the current produced by the element for a given amount of energy input. In this case, the quality of the fit is almost perfect. On the other hand, from Fig. 13(d), it can be seen that there is no relationship between $\mathcal{R}_V^a$ at medium frequencies and F_V (1 kHz), indicating the irrelevance of this FoM to average responsivity in this case. There are 120 possible graphs of this type for the range of parameters chosen for the study. This is far too many to look at individually, but we can tabulate the values of R^2 and look at which graphs give values in excess of 75%. Anything less than this is poor correlation and indicates that the relevant

TABLE III. Tabulation of the parameters used to model the dielectric data for the materials chosen for the device performance modeling described in the text.

Material name	Material code	Type	ε'_K	f_e	a	b	σ_o	f_o	α	β
				Hz			Sm^{-1}	Hz		
$LiTaO_3$ (Congruent)	LTO	Crystal	43.5	0	1	1	1.25×10^{-12}	7.82	1	1
Deuterated triglycine sulfate	DTGS	Crystal	26.3	0	1	1	2.40×10^{-9}	150	1	1
Poly(vinylidenefluoride-trifluoroethylene) Copolymer	P(70VDF–30TrFE)	Polymer	10.7	0	1	1	2.56×10^{-15}	2.3×10^{-5}	0.925	0.925
$Pb_{(1-x)}Ca_x[(Co_{½}W_{½})_yTi_{1-y}]O_3$; x = 0.27, y = 0.04; 1%Mn	PCT:Mn	Ceramic	196	10	1.1	0.35	1.80×10^{-9}	5	0.82	1
$Pb[Zr_{1-x-y}(Fe_{½}Nb_{½})_xTi_y]_{1-z}U_zO_3$,x = 0.2, y = 0.02,z = 0.005	PZFNTU	Ceramic	290	0.14	0.5	0.2	1.90×10^{-10}	0.1	1.05	0.6
x $Pb(In_{1/2}Nb–)O_3$−y$Pb(Mg_{1/3}Nb–)O_3$−(1−x−y) $PbTiO_3$−Mn; x = 0.23,y = 47 (111)	PIMNT:Mn (23/47/30) (111)	Crystal	570	0	1	1	1.50×10^{-10}	14	0.75	1.25
$xPb(In_{½}Nb_{½})O_3$−y$Pb[(Mg_{⅓}Nb_{⅔})_xTi_{1-x}]$ O_3-(1−x−y)PbTiO3; x = 0.41,y = 0.17 (001)	PIMNT41/17/42 (001)	Crystal	486	0	1	1	1.50×10^{-10}	2	0.8	1.27
91.5$Na_{½}Bi_{½}TiO_3$−8.5$K_{½}Bi_{½}TiO_3$ < 111>	91.5NBT–8.5KBT <111>	Crystal	230	440	0.2	0.5	1.57×10^{-10}	0.24	0.92	1

© Author(s) 2023

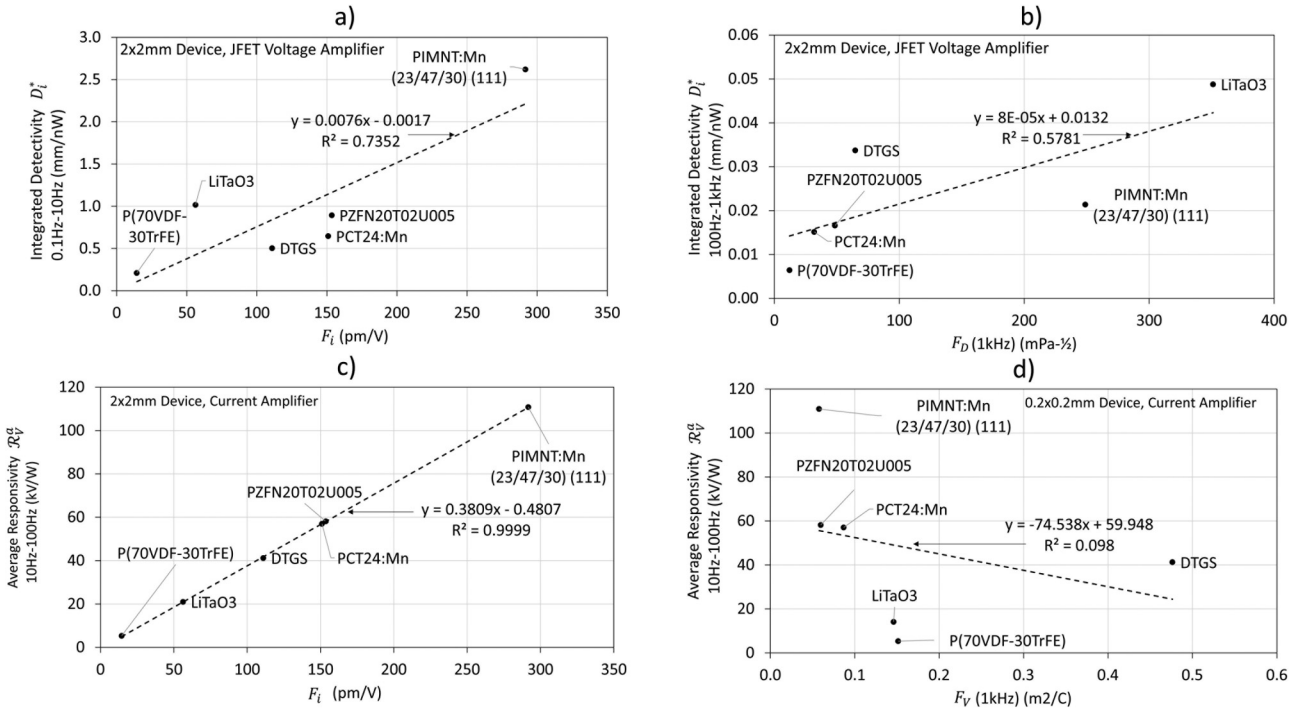

FIG. 13. Graphs of PIRD performance parameters plotted vs different pyroelectric figures-of-merit for six materials selected from Table I. The materials are LTO, DTGS, P(70VDF−30TrFE), PZFN20T02U005, PCT24:Mn, and PIMNT(23/47/30) (111). The graphs are (a) integrated detectivity D_i^* from 0.1 to 10 Hz plotted vs F_i for a 2 × 2 mm element JFET voltage amplified device; (b) D_i^* from 100 Hz to 1 kHz plotted vs F_D for a 2 × 2 mm element, JFET device; (c) average responsivity R_V^a from 10 Hz to 100 Hz plotted vs F_i for a 0.2 × 0.2 mm element OpAmp current amplified device; (c) average responsivity R_V^a from 10 Hz to 100 Hz plotted vs F_V for a 0.2 × 0.2 mm element current amplified device. Further device parameters are given in the text.

FoM is not going to give a good measure for how well a device using this material would perform against the particular performance measures chosen. The results of this analysis are shown in Table IV.

The first thing to note from this table is that there is great deal of blank space, implying that for most sets of conditions, the device performance parameters chosen are poorly correlated with the three FoMs. Of the three, F_i correlates the best with device performance. It shows strong correlation with predicted performance for the small-area elements using both types of amplifiers. This is to be expected, because of the direct link between F_i and the pyroelectric current for a given amount of energy input, especially as volume specific heat does not vary strongly between different materials. For small area devices, it is desirable to have as much current produced by the element as possible, regardless of the amplifier type. It is striking that it works well with the voltage amplified device on both measures of performance at all frequencies, although it does not work well for the current amplified device at medium and high frequencies. For the 2 × 2 mm element with a voltage amplifier, F_i works poorly ($R^2 < 75\%$) at all frequencies. With a current amplified device, it gives good-to-excellent correlation with responsivity but poor correlation with integrated detectivity. F_V works as a good FoM only for the average responsivities of the larger-area voltage amplified devices at medium-to-high frequencies, as would be expected.[13] F_D works with moderate correlation for the larger-area voltage amplified devices at medium frequencies and for the current amplified devices with both larger and smaller element areas at medium frequencies, with the strongest correlation for the smaller area devices, as would be expected from the argument given above. The only moderate correlation ($R^2 < 90\%$) with F_D for the larger area devices in this frequency band is presumably because the *tanδ* noise does not play such a large role in determining overall noise levels. Given that PIRDs are used most-commonly in the lower frequency band and most devices manufactured use areas in the square mm range with voltage amplifiers, the message from Table IV is that the three FoMs generally used by the pyroelectric materials community are, unfortunately, of dubious overall utility. One positive message for the community is that in the restricted areas where F_V and F_D are actually useful, values computed with the 1 kHz dielectric properties are just as useful as those computed with dielectric properties measured at lower frequencies. However, it must be emphasized that the measurement of lower frequency dielectric data is still needed. The evidence presented earlier in this paper has indicated strongly that having full-frequency dielectric data is very important if accurate predictions of device performance are to be made. Also, even though values of F_V

© Author(s) 2023

TABLE IV. Tabulation of the of R^2 values for the linear correlations between the integrated detectivities D_i^* and the average voltage responsivities R_V^a over the low, medium, and high frequency bands (defined in the table and text) and the three figures-of-merit F_i, F_V and F_D for 2 × 2 mm and 0.2 × 0.2 mm PIRDs (see text for a full description). F_V and F_D have been computed for dielectric properties measured at 1 kHz and 32 Hz (shown, respectively, as the two values separated by "/"). The cells are shaded as follows: darkest for $R^2 \geq 90\%$, for which correlation is the strongest and medium for $75\% \leq R^2 \leq 90\%$. Any correlation graph for which $R^2 < 75\%$ has been left blank, because such a low value implies too weak a correlation for the FoM to be useful in those circumstances.

Element area (mm)	2 × 2	0.2 × 0.2	2 × 2	0.2 × 0.2
F_i	JFET amplifier		Current amplifier	
Integrated detectivity 0.1–10 Hz	–	0.99	–	0.90
Integrated detectivity 10–100 Hz	–	0.99	–	–
Integrated detectivity 100 Hz–1 kHz	–	0.90	–	–
Average responsivity 0.1–10 Hz	–	0.94	1.00	0.97
Average responsivity 10–100 Hz	–	0.89	1.00	1.00
Average responsivity 100 Hz–1 kHz	–	0.86	0.81	0.81
F_V (1 kHz/32 Hz)	JFET Amplifier		Current Amplifier	
Integrated detectivity 0.1–10 Hz	–	–	–	–
Integrated detectivity 10–100 Hz	–	–	–	–
Integrated detectivity 100 Hz–1 kHz	–	–	–	–
Average responsivity 0.1–10 Hz	–	–	–	–
Average responsivity 10–100 Hz	0.99/0.99	–	–	–
Average responsivity 100 Hz–1 kHz	0.99/0.99	–	–	–
F_D (1 kHz/32 Hz)	JFET amplifier		Current amplifier	
Integrated detectivity 0.1–10 Hz	–	–	–	–
Integrated detectivity 10–100 Hz	0.88/0.77	–	0.86/0.75	0.94/0.87
Integrated detectivity 100 Hz–1 kHz	–	–	–	–
Average responsivity 0.1–10 Hz	–	–	–	–
Average responsivity 10–100 Hz	–	–	–	–
Average responsivity 100 Hz–1 kHz	–	–	–	–

and F_D computed from 1 kHz dielectric properties are as useful in comparing different materials as those calculated using low frequency dielectric properties, it is always wise to check that the dielectric loss does not rise rapidly at low frequencies. Another important message to take from Table IV is that it is inappropriate to over-emphasize the importance of increasing p/ε (to increase F_V) or reducing $tan\delta$ (to increase F_D) if this is at the expense of the pyroelectric coefficient (which determines F_i). In the end, making generalized statements on the basis of the pyroelectric FoMs alone can lead to poor material development and selection decisions. The only way to determine properly whether any pyroelectric material is going to be useful in each pyroelectric application is to use the right models and full-frequency dielectric data to calculate the device performance parameters in the frequency ranges of most interest.

V. OTHER CONSIDERATIONS

Material selection decisions are seldom made based purely upon device radiometric performance. Other considerations of how a pyroelectric material will affect device manufacturability and usability are also very important. A particularly clear example of this was cited above and in Fig. 12, taken from the work by Neumann *et al.*[96] in the comparison of the performances of LTO and PIMNT:Mn (23/47/30) (111) in PIRDs. The devices using PIMNT:Mn (23/47/30) (111) performed much better than those based on LTO, especially at low frequencies, by >5× in peak responsivity and >3× in peak detectivity. However, the detectivity advantage of PIMNT:Mn (23/47/30) (111) is lost above about

TABLE V. Integrated detectivities D_i^* (in units of mm/nW) over low (0.1–10 Hz), medium (10–100 Hz), and high (100 Hz–1 kHz) frequency ranges for 4 different materials selected from table I. The device design parameters are the same as those used for the FoM correlation calculations. The material properties are taken from tables I and IV.

Material	Amplifier type	2 × 2 mm elements Low	Med	High
LTO	Voltage	1.017	0.373	0.049
PIMNT:Mn (23/47/30) (111)	Current	1.930	0.325	0.014
PIMNT (41/17/42) (001)	Current	1.437	0.219	0.012
91.5NBT–8.5KBT <111>	Current	0.866	0.116	0.010
		0.2 × 0.2 mm elements		
LTO	Voltage	0.006	0.034	0.013
LTO	Current	0.025	0.036	0.014
PIMNT:Mn (23/47/30) (111)	Current	0.384	1.247	0.436
PIMNT (41/17/42) (001)	Current	0.304	0.927	0.254
91.5NBT–8.5KBT <111>	Current	0.289	0.713	0.135

© Author(s) 2023

160 Hz, and while the current amplifier is definitely the best option for the PIMNT:Mn (23/47/30) (111), it may not necessarily be the best option for LTO, as will be discussed below.

Table V gives the integrated detectivities D_i^* over low (0.1–10 Hz), medium (10–100 Hz), and high (100 Hz–1 kHz) frequency ranges for 2×2 mm and 0.2×0.2 mm devices using LTO and PIMNT:Mn (23/47/30) (111). In this case, the device design parameters are the same as those used for the FoM correlation calculations. A JFET voltage amplifier has been chosen for LTO, while the other materials in the table are used with current amplifiers because they are much higher permittivity materials. In this sense, the amplifiers have been chosen to best-suit the materials concerned. The material properties are taken from Tables I and IV.

In this case, for 2×2 mm detectors, the advantage of PIMNT:Mn (23/47/30) (111) in the low frequency band is clear, although the improvement is only about 90%, and not the factor-of-three we would see by only looking at peak detectivity. There is no advantage in the medium frequency band, and in the high frequency band, LTO is much better. For the small area (0.2×0.2 mm) detectors, PIMNT:Mn (23/47/30) (111) in the current mode is much better than LTO in voltage or current modes at all frequencies.

If we only look at the FoMs for these two materials, then the comparison of the ratio of F_i for these two materials indicates a 5× improvement for PIMNT:Mn relative to LTO, while the consideration of the F_D ratio alone would have indicated that LTO was 2.5× better than PIMNT:Mn (23/47/30) (111), or consideration of the F_V ratio alone would have indicated that LTO was 41% better than PIMNT:Mn (23/47/30) (111). These do not give a good indication of the relative performances of the materials in the different devices. This reinforces the "health warning" given above about the use of pyroelectric FoMs. The PIMNT:Mn (23/47/30) (111) devices reported by Neumann *et al.*[96] clearly showed very good performance. Nevertheless, the authors point out the potential problems associated with the use of this material in commercial devices. These include changes in material processing associated with material mechanical properties, the difficulties of keeping processing temperatures below 100 °C to avoid exceeding T_d (see Table I), material and device production costs, and the variations in composition and properties along the crystal boule growth axis, which limit the amount of a boule that can be used while keeping device uniform in performance. There are also likely to be issues for the end-users of PIMNT:Mn devices in keeping device temperatures below 100 °C in both system fabrication (e.g., during flow soldering processes) and use. The overall conclusion from this paper is that LTO remains "*the material of choice for the majority of demanding applications using thermal infrared detectors.*"[96]

This is not to say that an alternative pyroelectric material cannot be developed that will ultimately beat LTO in the PIRD application. On the contrary, the results from the PIMNT:Mn23/47/30 (111) devices are very encouraging, and if a similar material can be developed, which has the advantage of very high pyroelectric coefficient, without the manufacturing and use problems referred to above, that would be of great interest to the PIRD community. There is evidence that T_d can be raised significantly in this system, as PIMNT41/17/42 (001) shows a T_d of 253 °C, compared with 115 °C for PIMNT:Mn23/47/30 (111) while only showing modest (ca. 26%) reductions in the pyroelectric coefficient and F_i (see Table I). F_D is significantly (4×) lower. The predicted integrated detectivities D_i^* for this material when used in the selected device structures in low, medium, and high frequency bands are given in Table V. While not being as good as PIMNT:Mn23/47/30 (111), it would give about a 44% improvement in a 2×2 mm device relative to LTO at low frequencies but be significantly worse at medium and high frequencies. It would be a good deal better than LTO in the small area detectors. Whether the low frequency improvement would be sufficiently interesting to a device manufacturer to embark upon an expensive device development program to use the material is a moot point, and of course, improving T_d would not change issues like material uniformity and handleability. Nevertheless, there appears to be considerable promise in the PIMNT system. Doubling the detectivity relative to the current generation of devices through better pyroelectric material properties would have a direct knock-on to ultimate system performance and could be used either to simplify and cost-reduce system design (through, e.g., allowing the use of simpler, lower-cost optics) or to improve system performance (e.g., through improving detection range).

Over the last thirty years or so, there has been increasing pressure on the electronics industry to remove lead from its products because of the extreme toxicity of the metal and the cumulative effects in the human body. There has been increasing pressure on the piezoelectric ceramics community to develop lead-free alternatives to the almost-ubiquitous use of lead zirconate titanate (PZT)-based compositions in piezoelectric products, leading to a substantial amount of research in field, which has been valued as being ca $400 M in the last 20 years.[109] So far, in spite of this extensive research,[110,111] there have been no credible alternatives developed that can replace PZT, for most applications. Hence, the piezoelectrics industry has continued to use PZT, by operating under a succession of time-limited exemptions from the various tranches of legislation that would, otherwise, eliminate its use. It can be seen from Table I that a substantial number of the technologically interesting pyroelectric materials are lead containing. Hence, there has been an awareness of the need for lead-free pyroelectric materials and an increasing number of papers have been published in the last 15 years in this topic area.[112] Nevertheless, it should be remembered that one of the best and most-popular pyroelectric materials (LTO) is lead-free in any case. At least one manufacturer (Nippon Ceramic) no longer makes PIRDs based on PZT ceramic. It is not known if this is due to the lead-containing issue, but it is interesting that the devices that have replaced them in their catalogue are LTO-based PIRDs manufactured by Panasonic, and the datasheets for these devices make a positive-play about the fact that the devices do not contain lead.

Some of the more-promising new lead-free materials, as based on their pyroelectric coefficients and FoMs, have been compositions based on $Na_{½}Bi_{½}TiO_3$ (see Table I). One of these has been chosen for further study here because of a combination of its good FoMs (especially F_i) and having a T_d of 153 °C, which is higher than most of the PIMNT family and perhaps at a level, which might not cause undue concern in fabrication and use, although one would probably be looking for $T_d > 200$ °C to be safe under device flow-soldering temperatures. The characteristics of PIRDs using 2×2 mm and 0.2×0.2 mm elements of a 91.5NBT–8.5KBT <111> single crystal material have been modeled using published

© Author(s) 2023

values of the pyroelectric and dielectric properties (including their frequency dependences).[82] The DC conductivity for pure NBT[113] was used in combination with these data to model the AC conductivity model parameters to produce the parameters given in Table IV. The results for the integrated detectivities based on the use of a current-amplifier are listed in Table V, to permit comparison with the other materials modeled. For mm-scale elements, the low frequency performance is comparable with (although ca. 15% less than) the LTO-based device used in the voltage mode, but the performance at medium and high frequencies is considerably worse. The material appears to have characteristics, which would make it favorable as a lead-free material if used in small element detectors, where its performance is considerably better than LTO, primarily because of its high pyroelectric coefficient.

VI. CONCLUSIONS

This article has presented detailed mathematical models for the performances of PIRDs employing voltage and current amplifiers. It has demonstrated that these models can give excellent agreement with the published performance data for devices using a range of different pyroelectric materials. It has been shown that it is desirable to use full-frequency data for the dielectric properties of the pyroelectric materials if good agreement is to be obtained between the models and the actual performances. It has also been shown that the frequency dependence of the dielectric constant and loss can be accurately described using relatively simple models for the real part of the relative permittivity and the AC conductivity. An important message is that great care should be taken when using the standard pyroelectric FoMs to select the best prospective materials for use in practical devices. It has been known for a long time that these FoMs have restrictions on their validity; restrictions that are "hard-baked" into the FoMs because they are inherent to the way they are derived from the models of PIRD performance. This review has shown for the first time just how poor the correlation is between the performance parameters of practical devices using pyroelectric materials and the FoMs for those materials. The best thing that one can say about the FoMs is that they may be useful as a "rule-of-thumb" guide to material selection. For example, it is always a good idea to maximize the pyroelectric coefficient, and having a low dielectric constant (or relative permittivity) may also be a good idea, but having a high permittivity may not necessarily be a bad thing, especially if a current-amplifier can be used and/or one is intending to make devices with very small elements (in a 1D or 2D array, for example). It is generally a good idea to minimize the dielectric loss because of its effect on $tan\delta$ noise, but once it is driven down below a certain value, further reductions may not be beneficial because noise in the device may be dominated by other noise sources, depending on the details of the device design and the amplifier components used. There is a strong message here to researchers studying pyroelectric materials, which is that it is not sufficient simply to measure the dielectric properties at 1 kHz. This is a frequency that is almost irrelevant to the way in which PIRDs are used in practice. Most PIRDs will be used in the range of 0.1–10 Hz for motion sensing and at 1 Hz to a few tens of Hz for most other applications. For engineers to be able to accurately model the performance of PIRDs, they really need the dielectric property data to be measured at frequencies down to 0.1 Hz, if possible, even though measurements below a few tens of Hz are challenging, especially for low loss materials. At the very least, it is important to check that the dielectric loss is not rising rapidly below 100 Hz. On the other hand, it has been shown here that the FoMs F_V and F_D calculated using dielectric properties measured at 1 kHz are as useful in comparing different materials as those calculated using dielectric properties measured at a few tens of Hz. However, that must be viewed with the strong caveat that all three FoMs are of dubious utility other than as "rules-of-thumb," as stated above. Of the three FoMs, F_i is most useful in that it correlates best with overall device performance, but as most materials have very similar values of the volume specific heat, this is equivalent to saying the pyroelectric coefficient should be as large as possible, which is a reasonably obvious statement to make when talking about a pyroelectric device. Ideally, researchers in pyroelectric materials should measure and report full-frequency dielectric data so that they can be used in the models for device performance of the type presented here. These can be used to predict the likely utility of their materials in real devices. This should be done in preference to simply presenting FoMs calculated on the basis of dielectric properties measured at 1 kHz. However, it recognized that this might be a little onerous.

It is also important to make sure that a prospective material will be stable in use. This means that the depolarization temperature should not be too low, as, otherwise, there will be severe restrictions on the way the material can be processed into devices and/or used in practice. We have seen here that a T_d of ca. 110 °C is probably too low to be comfortable for a device manufacturer. There are plenty of papers where very high pyroelectric coefficients are reported where the Curie temperature T_C is close to room temperature. Prospectively, such materials can be used under a DC bias field to stabilize the polarization in so-called "dielectric bolometer" mode.[13] $PbSc_{½}Ta_{½}O_3$ (PST)[114] and (Ba,Sr)TiO_3 (BST)[115] ceramics have been used in this way successfully and commercialized in thermal imagers. However, their use is quite specialized and dielectric bolometer materials have not made it into the large-scale commercial PIRD arena for mm-scale detectors. This is despite the fact that significant (more than 2×) improvements in D^* have been demonstrated (in PST) relative to more-conventional pyroelectric ceramics,[73] and is probably because of the complexity involved in providing the DC bias field and potential issues with the pyroelectric material properties ageing under high DC bias fields when applied for long periods of time.[73] Their high permittivities and high pyroelectric coefficients are also best suited to very small element detectors used in arrays with large element counts.

The vast majority of commercial PIRDs are now based on the use of LTO as the pyroelectric material. Of the new pyroelectric materials that have emerged in the last 15 years, the PIMNT-based materials are undoubtedly the best. The extensive (and heavily funded) research that has gone into these materials for their prospective use in piezoelectric applications has made relatively large (many cm linear dimensions) crystals available. It has also been shown that their excellent pyroelectric and dielectric properties translate into significantly improved PIRD performance in prototype devices when considered alongside LTO. However, these materials bring their own challenges of a relatively low depolarization

© Author(s) 2023

temperature, materials uniformity and difficulties of processing and handling, especially when compared with LTO. There is evidence that the depolarization temperature can be improved, although the results presented here indicate that this is at the expense of some PIRD performance. Nevertheless, the PIMNT-based materials have an excellent combination of electrical properties, especially the high pyroelectric coefficient, that make them particularly well suited to small-area elements of the type that are used for 1D and 2D arrays. It remains to be seen whether these materials will ever make it into commercially available devices that can be used by system manufacturers. Of the best new lead-free materials reported, there are none that can yet compete on performance with LTO (which is also lead-free) for mm-scale detectors, although they would be significantly better than LTO for small-area detectors if used in the current-mode. Such small area detectors would be usefully applied in linear and 2D arrays.

SUPPLEMENTARY MATERIAL

See the supplementary material for a figure describing the input referred voltage noise ($\overline{e_n}(f)$) of two commercial JFET devices and a table of some commercially available PIRDs.

ACKNOWLEDGMENTS

The funding of this work by Innovate UK and RCUK under the SMART Grant "WILDFIRE: Enhanced PIRD sensors for remote wildfire detection and prevention" under Project No. 96321 is gratefully acknowledged. The device photographs in Fig. 2 were kindly provided by Mr. C. Carter.

AUTHOR DECLARATIONS

Conflict of Interest

The authors have no conflicts to disclose.

Author Contributions

Roger W. Whatmore: Conceptualization (lead); Data curation (lead); Formal analysis (lead); Methodology (lead); Project administration (lead); Supervision (lead); Visualization (lead); Writing – original draft (lead); Writing – review & editing (lead). **Samuel J. Ward:** Formal analysis (supporting); Investigation (supporting); Methodology (supporting).

DATA AVAILABILITY

The data that support the findings of this study are available from the corresponding author upon reasonable request.

REFERENCES

[1]A. Shaulov, Appl. Phys. Lett. **39**, 180–181 (1981).
[2]A. Shaulov, W. A. Smith, and N. V. Rao, Ferroelectrics **38**, 967–970 (1981).
[3]S. B. Lang, Ferroelectrics **230**, 99 (1999).
[4]Y. Ta, Compt. Rend. Acad. Sci. **207**, 1042 (1938).
[5]L. J. Sivian, USA patent, 2,999,260 (Bell Telephone Laboratories Inc., 1942).
[6]T. M. Lee, A. P. Anderson, and F. A. Benson, Electron. Lett. **22**, 200 (1986).
[7]J. R. Alday, IEEE Trans. Electron Devices **16**, 598–601 (1969).
[8]C. L. Wang, J. M. Auerbach, J. D. Eckels, J. C. Koo, H. N. Kornblum, D. F. Price, J. A. Smith, and S. C. Stotlar, Rev. Sci. Instrum. **57**, 2177–2178 (1986).
[9]D. K. Killinger, J. H. Churnside, and L. S. Rothman, *Atmospheric Optics, OSA Handbook of Optics* (McGraw-Hill, 1995), Chap. 44.
[10]C. B. Roundy and R. L. Byer, J. Appl. Phys. **44**, 929–931 (1973).
[11]K. Hashimoto, K. Morinaka, N. Yoshiike, C. Kawaguchi, and S. Matsueda, in *Proceedings of International Solid State Sensors and Actuators Conference (Transducers '97) Volume 2* (Elsevier Science, Lausanne, Switzerland, 1997), p. 1291.
[12]D. E. Dausch, S. H. Goodwin-Johansson, G. McGuire, L. E. Kramer, and M. R. Davidson, in *Proceedings of Infrared Technology and Applications XXVII: Aerospace/Defense Sensing, Simulation, and Controls (SPIE 4369)* (SPIE, 2001).
[13]R. W. Whatmore, Rep. Progr. Phys. **49**, 1335–1386 (1986).
[14]R. W. Whatmore and R. Watton, in *Infrared Detectors and Emitters Materials and Devices*, edited by C. T. Elliott and P. Capper (Kluwer Academic Publishers, The Netherlands, 2001), p. 99.
[15]S. O. Al-Jazzar, S. A. Aldalahmeh, D. McLernon, and S. A. R. Zaidi, IEEE Sens. J. **20**, 6075–6082 (2020).
[16]Y.-W. Bai and Y.-T. Ku, IEEE Trans. Consumer Electron. **54**, 1173–1176 (2008).
[17]I. V. Sherstov and D. B. Kolker, Quantum Electron. **50**, 1063–1067 (2020).
[18]C. F. Carter and N. Cross, Meas. Sci. Technol. **14**, 1117–1122 (2003).
[19]J. Yang, B. Chen, J. Zhou, and Z. Lv, Sensors **15**, 19618–19632 (2015).
[20]A. Sixsmith, N. Johnson, and R. Whatmore, J. Phys. IV **128**, 153 (2005).
[21]A. J. Holden, IEEE Trans. Ultrason. Ferroelectr. Freq. Control **58**, 1981–1987 (2011).
[22]A. J. Holden, in *Infrared Technology and Applications Xxxix; Vol. 87041N*, edited by B. F. Andresen, G. F. Fulop, C. M. Hanson, and P. R. Norton (SPIE-International Society of Optical Engineering, Bellingham, 2013), p. 1.
[23]"Global Pyroelectric Infrared Sensor Market Report" (Cognitive Market Research, 2023), https://www.cognitivemarketresearch.com/pyroelectric-infrared-sensor-market-report#report_summary
[24]R. A. Hanel, J. Opt. Soc. Am. **51**, 220 (1961).
[25]J. Cooper, Rev. Sci. Instrum. **33**, 92–95 (1962).
[26]J. Lehman, E. Theocharous, G. Eppeldauer, and C. Pannell, Meas. Sci. Technol. **14**, 916–922 (2003).
[27]D. E. Marshall, J. C. Gelpey, J. W. Marciniec, A. M. Chiang, and R. B. Maciolek, "Improved Detectivity of Pyroelectric Detectors," Report No. NASI-14372 (National Aeronautics and Space Administration, 1978), see https://ntrs.nasa.gov/citations/19780025463.
[28]N. Shorrocks, R. W. Whatmore, M. Robinson, and S. Porter, in *1985 International Technical Symposium/Europe (SPIE 0588)* (SPIE, 1986), p. 44.
[29]J. H. Lehman, C. Engtrakul, T. Gennett, and A. C. Dillon, Appl. Opt. **44**, 483 (2005).
[30]C. Hilsum, J. Opt. Soc. Am. **44**, 188 (1954).
[31]M. Schossig, V. Norkus, and G. Gerlach, Infrared Phys. Technol. **63**, 35–41 (2014).
[32]E. H. Putley, J. Sci. Instrum. **43**, 857–868 (1966).
[33]E. H. Putley, Infrared Phys. **20**, 139–147 (1980).
[34]C. B. Roundy, R. L. Byer, D. W. Phillion, and D. J. Kuizenga, Opt. Commun. **10**, 374–377 (1974).
[35]W. Zhu, J. R. Izatt, and B. K. Deka, Appl. Opt. **28**, 3647 (1989).
[36]E. H. Putley, Infrared Phys. **20**, 149–156 (1980).
[37]A. Van der Ziel and S. T. Liu, Physica **61**, 589–593 (1972).
[38]J. F. Nye, *Physical Properties of Crystals: Their Representation by Tensors and Matrices* (Oxford University Press, 1957).
[39]S. E. Stokowski, Appl. Phys. Lett. **29**, 393–395 (1976).
[40]V. B. Samoilov and L. V. Shchedrina, Ferroelectrics **118**, 225–231 (1991).
[41]V. B. Samoilov and L. V. Shchedrina, Ferroelectrics **131**, 169–172 (1992).
[42]N. Neumann and S. Mohling, Infrared Phys. **34**, 487–499 (1993).
[43]R. W. Whatmore, Ferroelectrics **49**, 201–210 (1983).
[44]F. A. Levinzon, IEEE Trans. Circuits Syst. I: Fundamental Theory Appl. **47**, 981–985 (2000).

© Author(s) 2023

[45]F. A. Levinzon and L. K. J. Vandamme, Fluct. Noise Lett. **10**, 447–465 (2011).
[46]"Noise in Pyroelectric IR Detectors" (Laser Components, 2019), www.lasercomponents.com.
[47]"InfraTec Pyroelectric Library," (Laser Components, 2012), www.lasercomponents.com.
[48]"JFE150 Ultra-Low-Noise, Low-Gate-Current, Audio, N-Channel JFET Datasheet" (Texas Instruments, 2021).
[49]Q. Xu, X. Zhao, X. Li, H. Deng, H. Yan, L. Yang, W. Di, H. Luo, and N. Neumann, Infrared Phys. Technol. **76**, 111–115 (2016).
[50]G. B. Clayton and S. Winder, *Operational Amplifiers* (Elsevier, 2003).
[51]J. Graeme, *Photodiode Amplifiers: Op Amp Solutions* (McGraw-Hill, Inc., 1995).
[52]D. Zhang, H. Wu, C. R. Bowen, and Y. Yang, Small **17**, 2103960 (2021).
[53]G. A. Burdick and R. T. Arnold, J. Appl. Phys. **37**, 3223–3226 (1966).
[54]S. T. Liu, Ferroelectrics **10**, 83–89 (1976).
[55]S. Leng and Y. Yu, Phys. Stat. Sol. (a) **143**, 431–439 (1994).
[56]P. Felix, P. Gamot, P. Lacheau, and Y. Raverdy, Ferroelectrics **17**, 543–551 (1977).
[57]F. J. Romero, M. C. Gallardo, J. M. Martin-Olalla, and J. del Cerro, J. Appl. Phys. **107**, 124110 (2010).
[58]R. B. Lal and A. K. Batra, Ferroelectrics **142**, 51–82 (1993).
[59]M. Polomska, B. Hilczer, and M. Michalczyk, Ferroelectrics **39**, 1217–1220 (1981).
[60]W. Shi, M. Wang, X. Sun, Q. T. Gu, H. S. Zhuo, and C. S. Fang, Progr. Cryst. Growth Charact. Mater. **40**, 293–299 (2000).
[61]R. B. Olsen, D. A. Bruno, J. M. Briscoe, and E. W. Jacobs, J. Appl. Phys. **58**, 2854–2860 (1985).
[62]N. Neumann, R. Kohler, and G. Hofmann, Ferroelectrics **118**, 319–324 (1991).
[63]W. Vonmunch, M. Nagele, M. Rinner, G. Wohl, B. Ploss, and W. Ruppel, Sens. Actuators A: Phys. **37–38**, 365–369 (1993).
[64]N. Neumann and R. Kohler, Proc. SPIE Infrared Technol. **2021**, 35–44 (1993).
[65]B. Martin, M. Mai, and H. Kliem, Phys. B: Condens. Matter **407**, 4398–4404 (2012).
[66]C. S. Daily, W. Sun, M. R. Kessler, X. Tan, and N. Bowler, IEEE Trans. Dielectr. Electr. Insul. **21**, 488–496 (2014).
[67]R. W. Whatmore, P. Kirby, A. Patel, N. M. Shorrocks, T. Bland, and M. Walker, in *Proceedings of NATO Conference on Science and Technology of Electroceramic Films, E284*, 1994, Villa del Mare, Italy (Kluwer Academic Publishers, Dordrecht, 1994), p. 383.
[68]M. M. Nadoliisky, T. K. Vassileva, and R. V. Yanchev, Ferroelectrics **118**, 111–115 (1991).
[69]J. de Frutos and B. Jiménez, Sens. Actuators A: Phys. **32**, 393–395 (1992).
[70]N. Ichinose, Y. Hirao, M. Nakamoto, and Y. Yamashita, Jpn. J. Appl. Phys. **24**, 178 (1985).
[71]M. Kobune, A. Mineshige, S. F. Fujii, and Y. Maeda, Jpn. J. Appl. Phys. **36**, 5976 (1997).
[72]R. W. Whatmore and F. W. Ainger, Proc. Soc. Photo-Opt. Instrum. Eng. **395**, 261 (1983).
[73]R. W. Whatmore, S. B. Stringfellow, and N. M. Shorrocks, Infrared Technol. XIX **2020**, 391 (1993).
[74]P. P. Donohue, "Annealing studies of detector materials for uncooled thermal imaging," Ph.D. thesis (University of Southampton, 2001).
[75]Y. Tang and H. Luo, J. Phys. D: Appl. Phys. **42**, 075406 (2009).
[76]Q. Xu, X. Zhao, W. Di, L. Li, L. Yang, X. Li, B. Ren, J. Jiao, H. Luo, and L. Shi, Infrared Phys. Technol. **67**, 350–353 (2014).
[77]H. Ursic, M. Vrabelj, L. Fulanovic, A. Bradesko, S. Drnovsek, and B. Malic, Inform. Midem-J. Microelectron. Electron. Comp. Mater. **45**, 260 (2015).
[78]F. Weyland, R. Perez-Moyet, G. A. Rossetti, and N. Novak, Energy Technol. **6**, 1512–1518 (2018).
[79]P. Yu, F. F. Wang, D. Zhou, W. W. Ge, X. Y. Zhao, H. S. Luo, J. L. Sun, X. J. Meng, and J. H. Chu, Appl. Phys. Lett. **92**, 252907 (2008).
[80]P. Yu, Y. Ji, N. Neumann, S. Lee, H. Luo, and M. Es-Souni, IEEE Trans. Ultrason. Ferroelectr. Freq. Control **59**, 1983–1989 (2012).
[81]Z. Liu, W. Ren, P. Peng, S. Guo, T. Lu, Y. Liu, X. Dong, and G. Wang, Appl. Phys. Lett. **112**, 142903 (2018).
[82]B. Zhang, R. Sun, F. Wang, T. Feng, P. Zhang, and H. Luo, J. Adv. Dielectr. **11**, 5 (2021).
[83]R. Sun, J. Wang, F. Wang, T. Feng, Y. Li, Z. Chi, X. Zhao, and H. Luo, J. Appl. Phys. **115**, 074101 (2014).
[84]C. C. W. Ruppel, IEEE Trans. Ultrason. Ferroelectr. Freq. Control **64**, 1390–1400 (2017).
[85]C. Winnewisser, P. U. Jepsen, M. Schall, V. Schyja, and H. Helm, Appl. Phys. Lett. **70**, 3069–3071 (1997).
[86]R. Watton, D. Burgess, and B. Harper, J. Appl. Sci. Eng., Sect. A Electr. Power Inform. Syst. **2**, 47 (1977).
[87]L. Garn and E. Sharp, IEEE Trans. Parts, Hybrids, Packag. **10**, 208–221 (1974).
[88]H. H. Wieder and C. R. Parkerson, J. Phys. Chem. Solids **27**, 247–252 (1966).
[89]K. L. Bye, P. W. Whipps, and E. T. Keve, Ferroelectrics **4**, 253–256 (1972).
[90]T. Furukawa, M. Date, E. Fukada, Y. Tajitsu, and A. Chiba, Jpn. J. Appl. Phys. **19**, L109–L112 (1980).
[91]R. Bruchhaus, D. Pitzer, M. Schreiter, and W. Wersing, J. Electroceram. **3**, 151–162 (1999).
[92]Q. Zhang and R. W. Whatmore, J. Appl. Phys. **94**, 5228 (2003).
[93]P. Wojtczuk, A. Armitage, T. D. Binnie, and T. Chamberlain, in *Proceedings of Sensor Devices 2011: The Second International Conference on Sensor Device Technologies and Applications*, 2011, Wilmington (Iaria Xps Press, 2011), p. 99.
[94]R. W. Whatmore, J. M. Herbert, and F. W. Ainger, Phys. Stat. Sol. (a) **61**, 73–80 (1980).
[95]T. R. Shrout, Z. P. Chang, N. Kim, and S. Markgraf, Ferroelectr. Lett. Sect. **12**, 63–69 (1990).
[96]N. Neumann, A. Kaiser, and D. Mutschall, APL Mater. **9**, 021106 (2021).
[97]A. K. Jonscher, Nature **267**, 673–679 (1977).
[98]R. W. Whatmore and A. J. Bell, Ferroelectrics **35**, 155–160 (1981).
[99]R. W. Whatmore, P. C. Osbond, and N. M. Shorrocks, Ferroelectrics **76**, 351–367 (1987).
[100]S. G. Porter, R. Watton, and R. K. McEwan, Proc. SPIE Infrared Technol. **2552**, 573–582 (1995).
[101]Y. Yamashita, K. Yokoyama, H. Honda, and T. Takahashi, Jpn. J. Appl. Phys. **20**, 183 (1981).
[102]B. Jiménez, J. M. Vicente, and R. Jiménez, J. Phys. Chem. Solids **57**, 389–396 (1996).
[103]J. Kuwata, K. Uchino, and S. Nomura, Jpn. J. Appl. Phys. **21**, 1298 (1982).
[104]S.-E. Park and T. R. Shrout, IEEE Trans. Ultrason. Ferroelectr. Freq. Control **44**, 1140–1147 (1997).
[105]M. Davis, D. Damjanovic, and N. Setter, J. Appl. Phys. **96**, 2811–2815 (2004).
[106]L. Liu, X. Wu, S. Wang, W. Di, D. Lin, X. Zhao, and H. Luo, J. Cryst. Growth **318**, 856–859 (2011).
[107]A. Movchikova, A. Günther, N. Neumann, and M. Heinze, Technisches Messen; Vol. 81 (2014), p. 120.
[108]E. W. Yap, N. Kumar, D. Damjanovic, R. Preston, and J. E. Daniels, J. Appl. Phys. **131**, 114503 (2022).
[109]A. J. Bell and O. Deubzer, MRS Bull. **43**, 581–587 (2018).
[110]H. Wei, H. Wang, Y. Xia, D. Cui, Y. Shi, M. Dong, C. Liu, T. Ding, J. Zhang, and Y. Ma, J. Mater. Chem. C **6**, 12446–12467 (2018).
[111]J. Wu, J. Appl. Phys. **127**, 190901 (2020).
[112]H. He, X. Lu, E. Hanc, C. Chen, H. Zhang, and L. Lu, J. Mater. Chem. C **8**, 1494–1516 (2020).
[113]K. S. Ojha, K. N. Singh, and P. K. Bajpai, in *16th National Seminar on Ferroelectrics and Dielectrics (NSFD)*, 2010, Bilaspur, India (American Institute of Physics, 2010), p. 154, Vol. 1372.
[114]N. M. Shorrocks, R. W. Whatmore, and P. C. Osbond, Ferroelectrics **106**, 387–392 (1990).
[115]B. M. Kulwicki, A. Amin, H. R. Beratan, and C. M. Hanson, in *Proceedings of the 8th IEEE International Symposium on Applications of Ferroelectrics* (IEEE, 1992), p. 1.

© Author(s) 2023